Precision imaging and nanoimmunotherapy for inflammatory atherosclerosis

Senders, M.L.

Publication date
2021

Chapter 4

Nanobody-facilitated multiparametric PET/MRI phenotyping of atherosclerosis

JACC Cardiovascular Imaging 12, 2015-2026 (2019)

Max L. Senders, Sophie Hernot, Giuseppe Carlucci, Jan C. van de Voort, Francois Fay, Claudia Calcagno, Jun Tang, Amr Alaarg, Yiming Zhao, Seigo Ishino, Anna Palmisano, Gilles Boeykens, Anu E. Meerwaldt, Brenda L. Sanchez-Gaytan, Samantha Baxter, Laura Zendman, Mark E. Lobatto, Nicolas A. Karakatsanis, Philip M. Robson, Alexis Broisat, Geert Raes, Jason S. Lewis, Sotirios Tsimikas, Thomas Reiner, Zahi A. Fayad, Nick Devoogdt, Willem J.M. Mulder, Carlos Pérez-Medina

Abstract

Objectives – This study sought to develop an integrative positron emission tomography (PET) with magnetic resonance imaging (MRI) procedure for accurate atherosclerotic plaque phenotyping, facilitated by clinically approved and nanobody radiotracers.

Background – Noninvasive characterization of atherosclerosis remains a challenge in clinical practice. The limitations of current diagnostic methods demonstrate that, in addition to atherosclerotic plaque morphology and composition, disease activity needs to be evaluated.

Methods – We screened 3 nanobody radiotracers targeted to different biomarkers of atherosclerosis progression, namely vascular cell adhesion molecule (VCAM)-1, lectin-like oxidized low-density lipoprotein receptor (LOX)-1, and macrophage mannose receptor (MMR). The nanobodies, initially radiolabeled with copper-64 (^{64}Cu), were extensively evaluated in Apoe$^{-/-}$ mice and atherosclerotic rabbits using a combination of in vivo PET/MRI readouts and ex vivo radioactivity counting, autoradiography, and histological analyses.

Results – The 3 nanobody radiotracers accumulated in atherosclerotic plaques and displayed short circulation times due to fast renal clearance. The MMR nanobody was selected for labeling with gallium-68 (^{68}Ga), a short-lived radioisotope with high clinical relevance, and used in an ensuing atherosclerosis progression PET/MRI study. Macrophage burden was longitudinally studied by ^{68}Ga-MMR–PET, plaque burden by T2-weighted MRI, and neovascularization by dynamic contrast-enhanced (DCE) MRI. Additionally, inflammation and microcalcifications were evaluated by fluorine-18 (^{18}F)-labeled fluorodeoxyglucose (^{18}F -FDG) and ^{18}F -sodium fluoride (^{18}F-NaF) PET, respectively. We observed an in- crease in all the aforementioned measures as disease progressed, and the imaging signatures correlated with histopathological features.

Conclusions – We have evaluated nanobody-based radiotracers in rabbits and developed an integrative PET/MRI protocol that allows noninvasive assessment of different processes relevant to atherosclerosis progression. This approach allows the multiparametric study of atherosclerosis and can aid in early stage anti-atherosclerosis drug trials.

Introduction

Atherosclerosis is an inflammatory disorder of the major arteries that is causative of cardiovascular disease (CVD)[1]. Lipid-driven progression of inflamed atherosclerotic lesions, initiated by vascular endothelium disruption, causes their development into plaques. In the process, inflammatory monocytes are recruited, which subsequently differentiate into macrophages that proliferate and evolve into foam cells[2,3]. Further progression is characterized by calcium depositions and additional lipid accumulation, resulting in plaque expansion with hypoxia-induced neovascularization[4]. Eventually, acute cardiovascular events like myocardial infarction (MI) and stroke may occur as a result of plaque erosion or rupture. Unfortunately, MI and sudden cardiac death are frequently the first signs of CVD in patients with otherwise a risk factor-free profile[5].

The limitations of current diagnostic methods demonstrate that, in addition to plaque morphology and composition, disease activity needs to be evaluated[6]. Over the past two decades, many different imaging approaches have been proposed to study the pathophysiological processes associated with atherosclerosis progression[7]. Positron emission tomography (PET) imaging with ^{18}F-fluorodeoxyglucose (^{18}F-FDG), for instance, is a clinically viable method to non-invasively quantify plaque inflammation[8-9]. However, ^{18}F-FDG lacks specificity as it is taken up by metabolically active cells, rendering imaging of the coronary arteries particularly challenging due to avid myocardial uptake[10]. More recently, ^{18}F-sodium fluoride PET (^{18}F-NaF-PET) has emerged as a promising method to visualize plaque microcalcifications[11]. Yet, due to the inherent limitations of standalone molecular imaging techniques, precise phenotyping of atherosclerotic lesions would profoundly benefit from an integrative multimodal imaging approach allowing simultaneous quantification of different key disease progression features. This would not only have a potential impact on future anti-atherosclerosis clinical drug trials[9], but is immediately relevant on a preclinical level, both for a better understanding of atherosclerosis biology and the development and evaluation of new drugs, noninvasively and longitudinally in animals.

The advent of fully integrated PET/magnetic resonance imaging (MRI) scanners brings together the strengths of the individual imaging modalities, i.e. MRI's excellent soft tissue contrast and real 3D imaging capabilities, and PET's sensitivity and radiotracer specificity. This synergy can be exploited advantageously for vessel wall imaging, as it allows accurate delineation of lesions and co-registration of functional information derived from the radiotracer's PET signal. In addition, MRI functional methods can be integrated to assess vessel wall permeability, as a measure of plaque neovascularization[12], and may be combined with vessel wall morphological assessment[13].

Here, we integrated nanobody radiotracer technology in a multiparametric PET/MR imaging protocol that allows precise characterization of the atherosclerotic plaque. Antibodies have been extensively used as PET/SPECT radiotracers, although long blood circulation times prohibit their use for vessel wall imaging. In contrast, nanobody-based

radiotracers are extremely well suited for this purpose, as their high affinity and specificity are similar to antibodies[14], but their markedly smaller size facilitates rapid blood clearance (figure 1A). Capitalizing on established work[15–17], we selected three nanobodies specific to different clinically relevant key markers of atherosclerosis progression[18], namely vascular cell adhesion molecule 1 (VCAM-1)[19], lectin-like oxidized low-density lipoprotein receptor 1[20] (LOX-1), and macrophage mannose receptor (MMR)[21] (figure 1B). These nanobodies, labeled with Copper-64 (^{64}Cu), were first extensively screened in Apoe$^{-/-}$ mice and atherosclerotic rabbits (figure 1C).

Finally, the MMR nanobody was further developed into a Gallium-68 (^{68}Ga)-labeled PET tracer. This tracer was then integrated in a multimodal protocol on a clinical PET/MRI system to simultaneously study vessel wall morphology and atherosclerotic plaque activity. The imaging protocol, involving ^{68}Ga-MMR nanobody-PET, anatomical and dynamic contrast enhanced MRI (DCE-MRI), in addition to ^{18}F-FDG- and ^{18}F-NaF-PET, was applied to study atherosclerosis progression in rabbits (figure 1C).

Results

Nanobody-radiotracer screening in mice

Nanobodies targeting three relevant markers of atherosclerosis progression[15–17] were screened for use in molecular imaging of atherosclerosis. A nanobody targeting myeloma protein (M-protein) was used as chemical control. The nanobodies were functionalized with the chelator NOTA. This modification was well tolerated, as the target affinity was retained (table S1). The nanobodies were radiolabeled with ^{64}Cu for preliminary in vivo screening in Apoe$^{-/-}$ mice, as this radioisotope allows extensive ex vivo evaluation due to its 12.7-hour decay half-life. Radiolabeling of all nanobodies proceeded in high radiochemical yield and purity (figure 1D). Biodistribution in Apoe$^{-/-}$ mice at 3 h post injection (p.i.) revealed high kidney uptake for all nanobodies, but with varying organ/tissue distribution patterns (figure 2A and table S2). Moreover, all nanobodies showed rapid blood radioactivity clearance with blood half-lives shorter than 2 minutes (figure S1). Autoradiography revealed preferential ^{64}Cu deposition at typical lesion sites like the aortic root for all radiotracers, while the control nanobody showed a homogeneous distribution pattern (figure 2B). Whole-aorta radioactivity concentration was highest for ^{64}Cu-MMR, as was the aorta-to-blood ratio (figure 2C). ^{64}Cu-MMR and ^{64}Cu-VCAM were selected for additional microPET/CT imaging, showing significant radioactivity accumulation in the aortic root and arch, where advanced lesions typically develop (figure 2D). Strong kidney and bladder signals were observed, indicative of fast renal clearance. Radiotracer cellular specificity in the plaque was assessed in sections taken from the aortic root of mice injected with the radiolabeled nanobodies. Autoradiography of aortic sections showed

co-localization of radioactivity with the expected cell types for each nanobody, i.e. endothelial cells for ^{64}Cu-VCAM, macrophages for ^{64}Cu-MMR, and both for ^{64}Cu-LOX, and immunofluorescence confirmed target specificity for all nanobodies[15-17] (figure 2E).

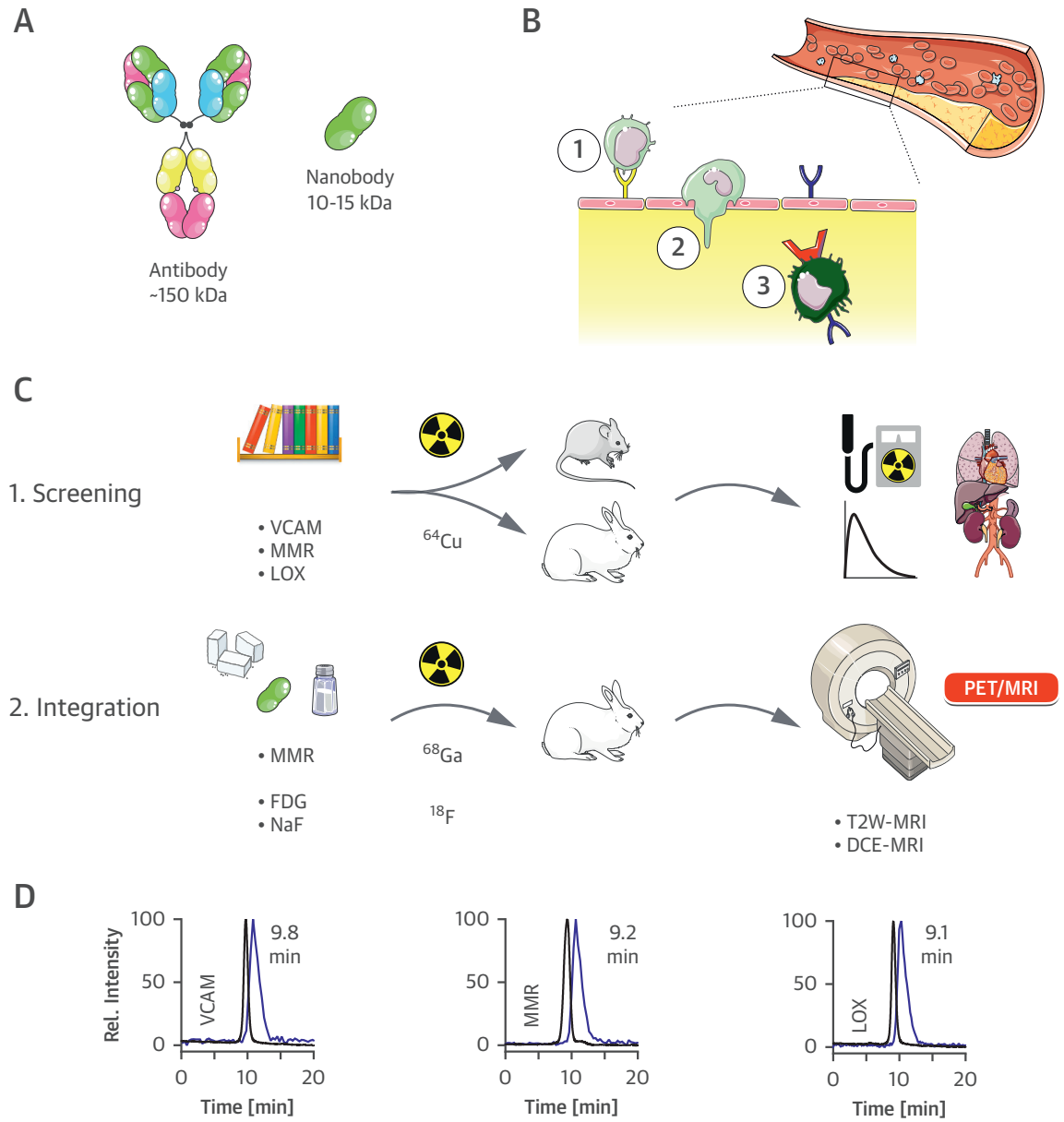

Figure 1. Nanobody-facilitated atherosclerosis PET imaging. A) Schematic representation of a full-size antibody and a nanobody. B) Monocyte/macrophage dynamics in atherosclerosis. Endothelial dysfunction is accompanied by the expression of the surface receptor LOX-1 (blue) or adhesion molecules like VCAM-1 (yellow). Circulating monocytes are recruited to atherosclerotic lesions via interaction with these adhesion molecules (1), leading to infiltration through the endothelium (2). Infiltrated monocytes eventually differentiate into macrophages (3), which may also express LOX-1 and the mannose receptor (MMR, red). C) Study outline. D) Size exclusion chromatograms of the three ^{64}Cu-nanobodies, demonstrating co-elution of radioactivity (blue trace) with the non-radioactive species (black trace, λ_{abs} = 220 nm).

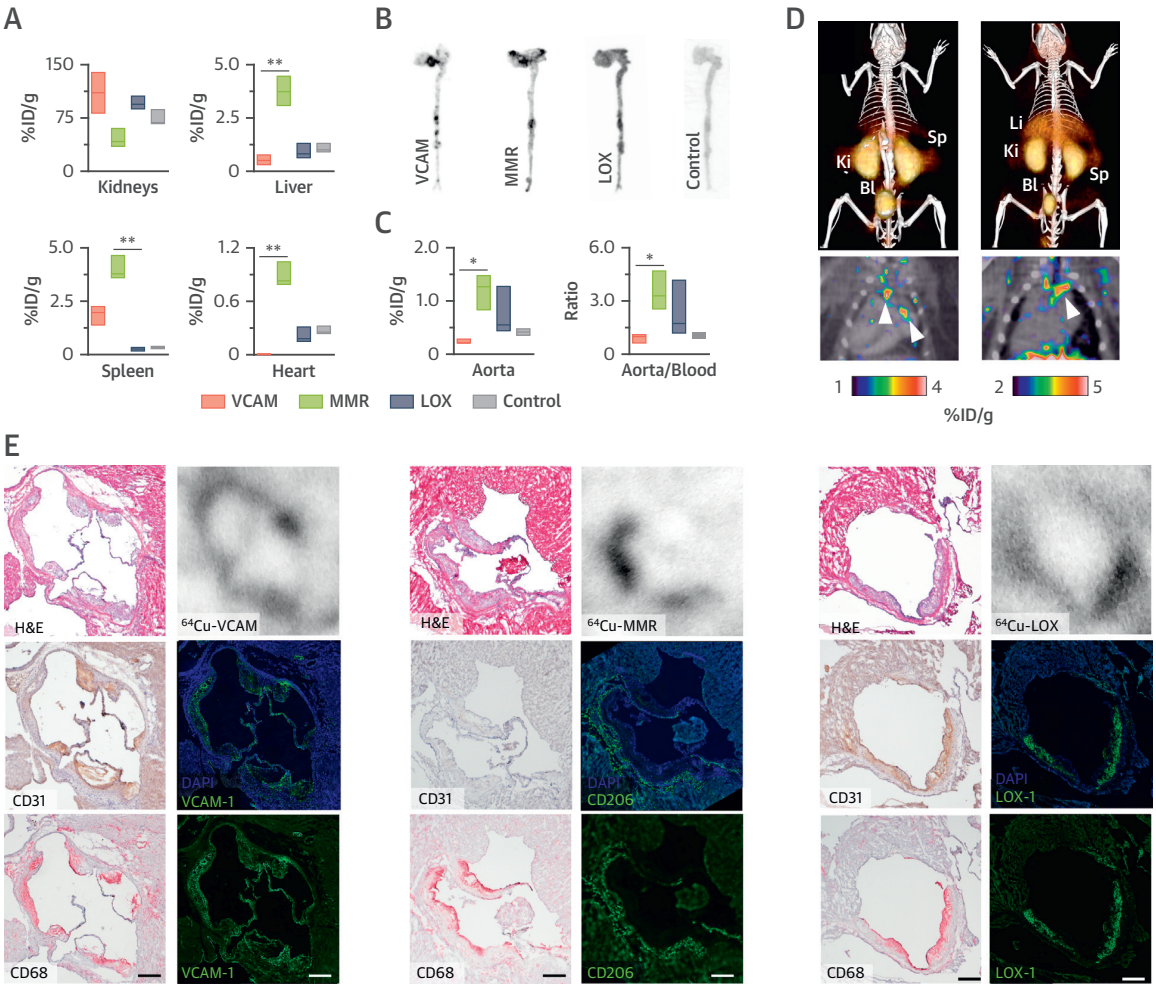

Figure 2. Nanobody-radiotracer screening in mice. A) Radioactivity distribution in selected tissues in Apoe$^{-/-}$ mice at 3 h p.i. of the corresponding ^{64}Cu-nanobody (n ≥ 3 per nanobody). B) Autoradiography and C) radioactivity concentration in aortas of Apoe$^{-/-}$ mice at 3 h p.i. of the corresponding ^{64}Cu-nanobody (n ≥ 3 per nanobody). D) Representative fused PET/CT images 1 h p.i. of ^{64}Cu-VCAM (left) and ^{64}Cu-MMR (right) in Apoe$^{-/-}$ mice. Arrows indicate enhanced uptake at the aortic arch and root, typical sites of atherosclerotic lesions. E) Representative images of aortic root sections from Apoe$^{-/-}$ mice with atherosclerosis showing, on the left column, hematoxylin and eosin (H&E) staining (top), and immunohistochemistry for CD31 (endothelial cells, middle) and CD68 (macrophages, bottom); on the right column, autoradiography (top), and immunofluorescence for the respective targets of the 3 nanobodies with (middle) and without (bottom) DAPI stain. Scale bar is 200 µm. * $P < 0.05$, ** $P < 0.01$. %ID/g = percentage injected dose per gram of tissue. Ki: kidney, Li: liver, Sp: spleen. Bl: bladder.

PET/MRI plaque phenotyping of rabbit atherosclerotic aortas

In vivo imaging experiments were conducted for the three ^{64}Cu-labeled nanobodies in a rabbit model of atherosclerosis using a clinical PET/MRI scanner (figure S2). A comprehensive in vivo PET/MRI analysis of atherosclerotic aortas of rabbits injected with the ^{64}Cu-nanobodies was carried out. In addition to nanobody-PET, the multimodal imaging protocol also included T2-weighted (T2W)-MRI measurement of vessel wall area (figure 3A, left) and dynamic contrast-enhanced (DCE)-MRI based evaluation of vascular

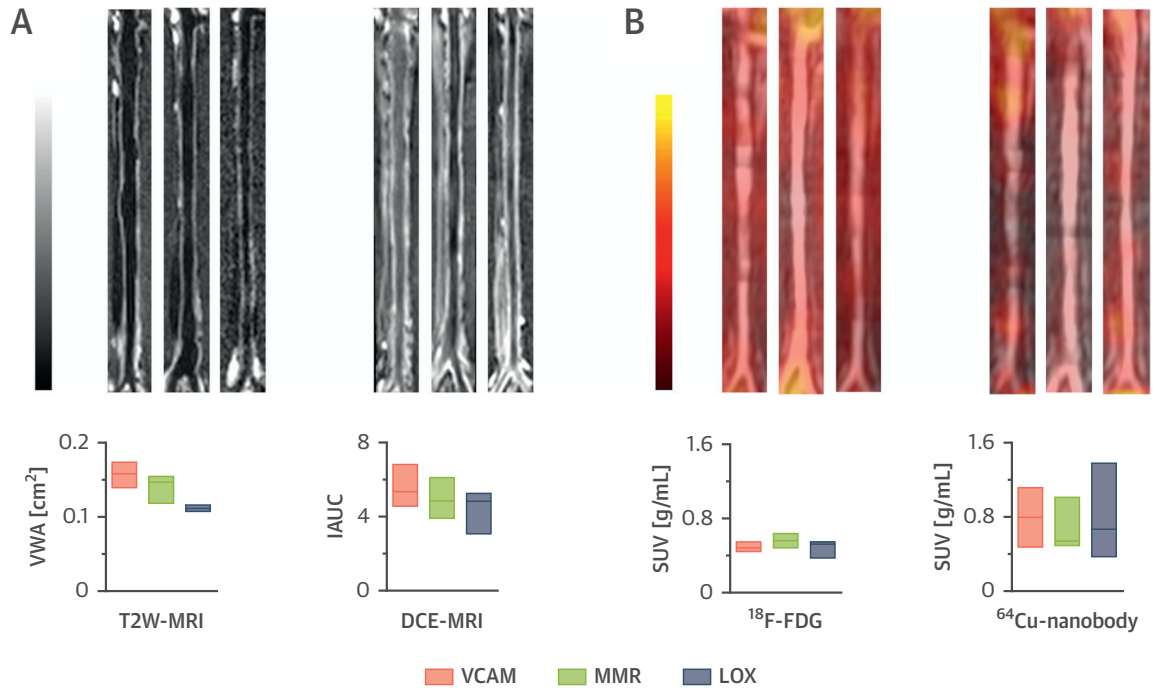

Figure 3. PET/MRI plaque phenotyping of rabbit atherosclerotic aortas. A) Representative T2W-MRI (left) and 3D DCE-MRI (right) images of aortas from rabbits with atherosclerosis. B) Representative coronal aortic PET/MR images at 3 h p.i. of ^{18}F-FDG (left), and at 160 min p.i. of ^{64}Cu-nanobody (right). In all panels, from left to right, images are shown for the ^{64}Cu-VCAM, ^{64}Cu-MMR, and ^{64}Cu-LOX groups. Below the images, from left to right: T2W-MRI vessel wall area (VWA), DCE-MRI permeability measurements (expressed as intensity area under the curve, IAUC, 2 min p.i. of contrast agent), and PET-derived radioactivity concentration for ^{18}F-FDG (3 h p.i.) and ^{64}Cu-nanobodies (160 min p.i.) in abdominal aortas from rabbits with atherosclerosis (n ≥ 4 per group).

permeability (figure 3A, right). Additionally, an ^{18}F-FDG-PET scan was performed two days before the nanobody-PET scan to allow direct comparison between ^{18}F-FDG and the nanobody radiotracers in the same rabbit (figure 3B, left). Representative PET/MR fusion images of aortas from rabbits injected with the ^{64}Cu-nanobodies recorded between 160-170 min p.i. are shown in figure 3B, right. T2-based plaque area, DCE-MRI measurements, and ^{18}F-FDG uptake were similar among the three groups of rabbits. Overall, these parameters suggest a similar degree of disease burden for all groups. Similar to the mouse studies, we found fast blood clearance with varying organ distributions by ex vivo gamma counting (figure S3A, B). Radioactivity concentration in the aorta, and aorta-to-muscle, aorta-to-blood and aorta-to-lung ratios were comparable for all nanobody radiotracers, while aorta-to-heart and aorta-to-liver ratios showed significant differences (figure S3C). In concordance with mouse findings, autoradiography of abdominal rabbit aortas showed a heterogeneous radioactivity distribution pattern for ^{64}Cu-VCAM and, especially, ^{64}Cu-MMR (figure S3D). The evaluation of a radiotracer's potential to discriminate atherosclerotic lesions from healthy segments in the vessel wall should take into account the disease's heterogeneity. Aorta-to-blood ratios are based on aortic value

averages from healthy and diseased segments. To better appreciate the nanobody tracers' atherosclerosis imaging potential, we conducted a careful autoradiographic analysis (figure S4A). The most diseased segments (MDS) had about 1.5, 3 and 4 times more counts per unit area than the corresponding atherosclerosis-free, least diseased segments (LDS) for ^{64}Cu-LOX, ^{64}Cu-VCAM and ^{64}Cu-MMR, respectively (Figure S4B and C). Moreover, MDS for ^{64}Cu-MMR contained more than two times the radioactivity per unit area than the average whole abdominal aorta (figure S4D). For illustrative purposes, we also computed MDS-to-blood and MDS-to-heart ratios (figure S4E and F). Collectively, these data suggest that the MMR nanobody has a high atherosclerosis imaging potential. A summary of the key findings from the ^{64}Cu-nanobody tracer studies in mice and rabbits can be found in Table 1.

Table 1. Key features of the ^{64}Cu-nanobody tracers described in this study. Data are expressed as median with interquartile range (IQR).

			^{64}Cu-VCAM	**^{64}Cu-MMR**	**^{64}Cu-LOX**
Target			Vascular cell adhesion molecule 1[19]	Macrophage mannose receptor[21]	Lectin-like oxidized LDL receptor 1[20]
Expressed on			Endothelial cells	Macrophages	Endothelial cells and macrophages
Mouse	Ex vivo	Aorta/blood ratio	1.0 (0.6-1.1)	3.3(2.6-4.7)	1.7 (1.3-3.6)
		Aorta/muscle ratio	7.3 (7.3-10.3)	3.0 (2.0-9.6)	2.3 (2.2-9.8)
Rabbit	PET	Aorta SUV_{max}	0.80 (0.53-1.11)	0.54 (0.50-0.78)	0.67 (0.41-1.07)
		Aorta/muscle ratio	6.0 (4.5-7.6)	5.5 (4.6-5.7)	5.7 (4.8-7.4)
	Ex vivo	Aorta/blood ratio	0.7 (0.6-1.0)	1.1 (0.8-1.3)	0.7 (0.4-1.7)
		Aorta/muscle ratio	4.5 (4.2-5.8)	4.7 (3.1-5.4)	2.9 (2.6-3.9)
		MDS*/blood ratio	1.2 (0.8-1.7)	2.3 (1.3-2.8)	0.9 (0.4-2.2)
		MDS*/heart ratio	4.0 (3.8-5.2)	3.2 (2.7-3.8)	2.5 (2.3-3.0)

*MDS: most diseased segment.

To investigate whether nanobody tracer accumulation was related to plaque size, inflammation or permeability, we performed extensive comparative region-by-region analyses between their uptake and the different parameters evaluated by our multipronged imaging protocol (figure S5). Interestingly, aortic ^{64}Cu-MMR uptake was not significantly correlated with ^{18}F-FDG's, but did show a positive correlation with vessel wall area (figure S5A). We also found a significant inverse correlation between ^{64}Cu-VCAM uptake and vessel wall area. Ex vivo radioactivity distribution in the aorta was evaluated by digital autoradiography and compared against the other parameters using a similar analysis (figure S6A). Importantly, significant correlations were found between PET-derived SUVs and radioactivity deposition as quantified from the autoradiographs for all ^{64}Cu-nanobodies, demonstrating the reliability of the imaging-derived values (figure S6B). No correlation was found between any ^{64}Cu-nanobody uptake and vascular

permeability, as measured by DCE-MRI, suggesting that their accumulation in the vessel wall is not governed by this parameter (figure S6C).

PET/MRI evaluation of atherosclerosis progression

Due to its favorable pharmacokinetics and plaque macrophage specificity, the MMR nanobody was further included in a PET/MRI atherosclerosis progression study. To match the nanobody's short blood circulation time and pursue a translational approach, in the ensuing experiments we used the shorter-lived isotope ^{68}Ga (physical half-life = 68 minutes). ^{68}Ga-MMR was obtained in high radiochemical yield and purity. Importantly, no meaningful differences were found between the ^{68}Ga-labeled VCAM and MMR nanobodies and their ^{64}Cu-labeled counterparts in preliminary experiments carried out in Apoe$^{-/-}$ mice (figure S7).

The study also included static ^{18}F-FDG and ^{18}F-NaF PET scans on consecutive days before the multiparametric ^{68}Ga-MMR PET/MRI session (figure S8A). We observed a gradual increase in ^{18}F-FDG and ^{68}Ga-MMR PET signal intensities in the aorta as disease progressed (figure 4A). Interestingly, while ^{18}F-NaF PET aortic signal was similar between controls and rabbits fed a cholesterol-enriched high-fat diet (HFD) for 4 months (4HFD), a significant increase after 8 months on HFD was found (8HFD). Aorta-to-muscle ratios showed a similar trend (figure S8B). Finally, vessel wall area and permeability also increased as disease advanced (figure 4B). Table S3 summarizes the main imaging parameters for the three tracers.

To explore the feasibility of coronary imaging, cardiac uptake for the three radiotracers was determined by PET to calculate the aorta-to-heart ratios in rabbits with advanced atherosclerosis (8HFD, figure 4C). ^{18}F-NaF showed the highest ratio due to its low uptake in cardiac tissue, followed by ^{68}Ga-MMR and ^{18}F-FDG, whose uptake in the myocardium was relatively high (SUV 2-4 g/mL) despite a 4-hour fasting protocol before injection. Similar to ^{64}Cu-MMR, vessel wall area was significantly associated with ^{68}Ga-MMR uptake ($r = 0.55$, $P = 0.0002$), indicative of macrophage accumulation in atherosclerosis progression. ^{68}Ga-MMR PET images were dominated by a strong kidney signal in all groups, and no significant differences were found in organ uptake for all tracers (kidney, liver, bone marrow –or bone for ^{18}F-NaF– and spleen) among the three groups (figure S8C). Ex vivo quantification of aortic uptake by gamma counting corroborated the in vivo findings (figure S8D, left). Marked differences in radioactivity deposition patterns were also observed between control and atherosclerosis groups by autoradiography (figure S8D, right). Of note, the blood half-life for ^{68}Ga-MMR was similar in all three groups (figure S8E).

Histological evaluation of aortic sections confirmed disease progression as shown by increased plaque area and macrophage content (figure 4D), as well as microcalcifications (figure S9A), in atherosclerotic aortas and absence of these hallmarks in the control and 4HFD group. Quantitative analysis revealed a significant increase in plaque size,

macrophage content and macrophage mannose receptor (CD206) expression as disease progressed (figure 5A and 5B). Importantly, CD206 immunostaining of diseased aortas correlated significantly with ^{68}Ga-MMR radioactivity measured by autoradiography (figure 5C). We found no CD206 staining in the control group, while in both atherosclerotic rabbit groups expression was observed (figure 5A and S9A). Of note, a significant correlation between macrophage content and our nanobody tracer was found in 4HFD rabbits, while in 8HFD rabbits the correlation weakened (figure S9B).

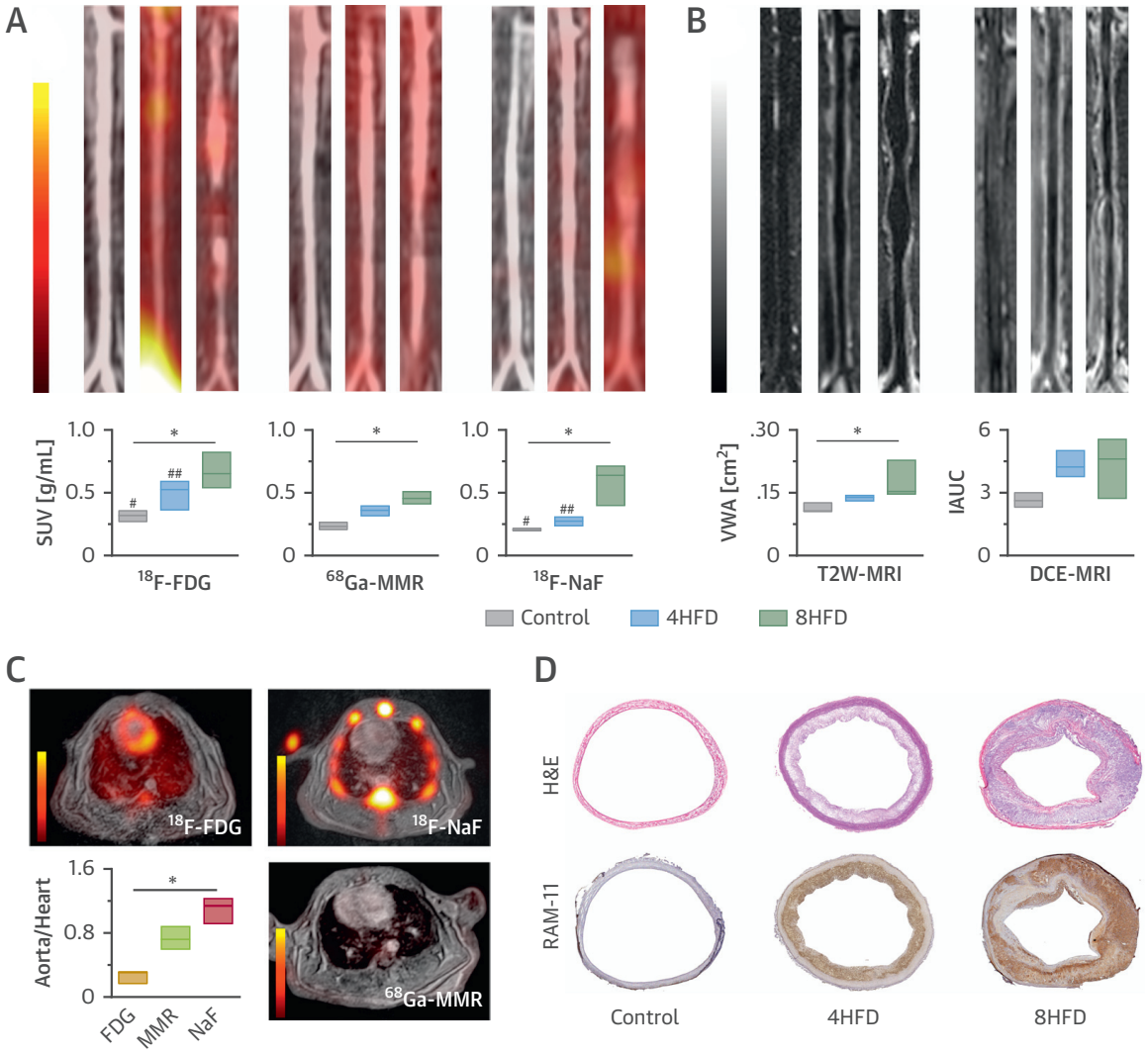

Figure 4. PET/MRI evaluation of atherosclerosis progression. A) Representative coronal aortic fused PET/MR images for ^{18}F-FDG (3 h p.i., left), ^{68}Ga-MMR (2 h p.i., middle) and ^{18}F-NaF (1.5 h p.i., right), and B) representative T2W-MRI (left) and DCE-MRI (right) images from healthy and atherosclerotic rabbits (4 or 8 months on high-fat diet, n ≥ 3 per group). C) Cardiac PET/MR images of the respective tracers and associated aorta-to-heart ratios in rabbits with atherosclerosis (8HFD). D) Aortic sections taken from healthy controls and atherosclerotic rabbits (4 or 8 months on a high-fat diet) and stained with hematoxylin and eosin (H&E) and RAM-11 (macrophages). * $P < 0.05$, ^{18}F-FDG vs. ^{18}F-NaF: $^{\#}$ $P < 0.05$, $^{\#\#}$ $P < 0.01$. VWA: vessel wall area. IAUC: intensity area under the curve.

In summary, using this multiparametric imaging protocol we were able to quantify different hallmarks of atherosclerosis in a non-invasive fashion. The observed imaging results were corroborated ex vivo by different techniques, demonstrating the robustness of this imaging approach to longitudinally evaluate disease burden.

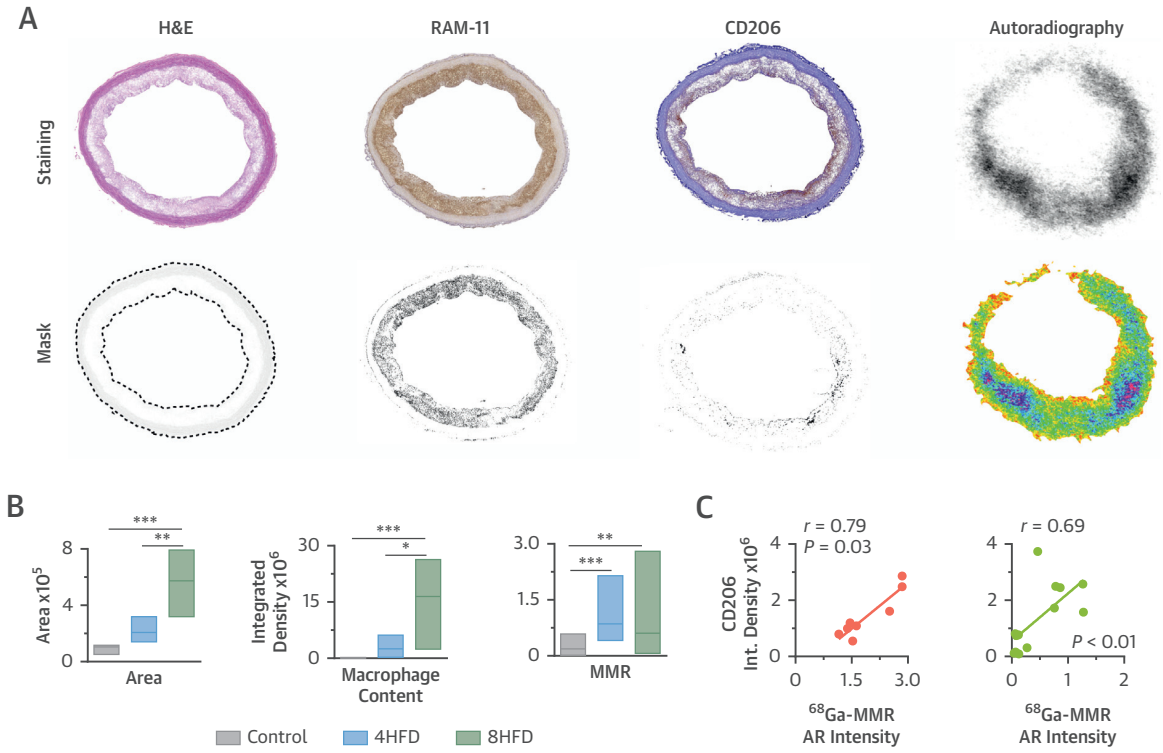

Figure 5. Ex vivo plaque characterization. A) Representative images of rabbit atherosclerotic aortic sections showing hematoxylin and eosin (H&E), RAM-11 (macrophages), and CD206 (MMR-expressing macrophages) staining, and the corresponding masks. B) Quantitative analysis in aortic sections, showing vessel wall area (left, based on H&E staining), macrophage content (middle, based on RAM-11 integrated density), and macrophage mannose expression (right, based on CD206 integrated density). C) Correlation between ^{68}Ga-MMR autoradiography (AR) and CD206 integrated density in aortic sections from atherosclerotic rabbits that had been 4 (red) and 8 months (green) on cholesterol-enriched high-fat diet. *** $P < 0.001$, ** $P < 0.01$, * $P < 0.05$.

Discussion

Three nanobodies targeting three well-established markers related to monocyte/macrophage dynamics were screened to identify key features of atherosclerotic lesions. In contrast to long-circulating full-size antibodies[22], the use of radiolabeled nanobodies enables PET vessel wall imaging at earlier time points due to their rapid blood clearance after injection. Conveniently, nanobodies' shorter circulation times allow their labeling with short-lived isotopes, substantially reducing radiation exposure. Indeed, in vivo PET/MRI biodistribution evaluation showed fast radioactivity clearance from blood that was mirrored by a rapid accumulation in the kidneys, confirming renal clearance for all nanobody tracers. Similar biodistribution patterns were observed in mice and rabbits.

However, whereas in rabbits there was no clear difference among aortic ^{64}Cu-nanobody uptakes, in Apoe$^{-/-}$ mice ^{64}Cu-MMR uptake was significantly higher. While this uptake can be attributed in part to MMR-positive cells in the adventitial layer and the surrounding perivascular tissue of atherosclerotic lesions of Apoe$^{-/-}$ mice[23], in rabbits we did observe an increased plaque uptake compared to controls and expression of the mannose receptor within the lesions. These observations likely reflect the differences in lesion composition between the two models[24]. Using our newly developed multiparametric atherosclerosis imaging protocol, we non-invasively observed a similar disease burden in all rabbits. Comparative analyses revealed a moderate correlation between vessel wall area and permeability, pointing to a certain degree of association between lesion size and neovascularization. Interestingly, while ^{64}Cu-VCAM uptake did not correlate with DCE-MRI permeability measurements, its uptake was negatively associated with vessel wall area, both in vivo and ex vivo. These findings are consistent with the distinct expression of VCAM-1 in early atherosclerotic lesions[25], and may warrant further research into the use of this VCAM-1 nanobody radiotracer to detect such lesions.

The MMR nanobody tracer was further included in an atherosclerosis progression study. To enhance translatability, and to match its short blood circulation half-life, we labeled the MMR nanobody with the clinically relevant[26], short-lived isotope ^{68}Ga. This facilitated a unique head-to-head comparison between clinically available radiotracers, namely ^{18}F-FDG and ^{18}F-NaF, and the MMR nanobody radiotracer. Image analysis revealed a significantly higher aortic uptake for ^{18}F-FDG, ^{18}F-NaF and ^{68}Ga-MMR in rabbits with advanced atherosclerotic lesions as compared to healthy controls, indicative of increased vessel wall (i) inflammatory activity, (ii) microcalcification, and (iii) macrophage burden, respectively. MR-based measurements also revealed an increase in vessel wall area and permeability. These findings are consistent with an increased plaque burden, although the three radiotracers seemed to accumulate at different locations and/or concentrations throughout the aorta as evidenced by the absence of significant correlations between their respective uptakes. This is in keeping with previous studies reporting a low degree of co-localization between ^{18}F-FDG and ^{18}F-NaF in atherosclerotic lesions[27]. Moreover, our histological and autoradiographic analyses of aortic sections showed no significant association between macrophage burden and mineral deposits. Taken together, these data are consistent with a temporal separation between the processes imaged by the two tracers, since macrophage-mediated inflammation and mineral deposition are considered hallmarks of early and advanced lesions, respectively. Therefore, these two tracers seem complementary and their combined use as a 'cocktail'[28] could be of value also in atherosclerosis.

The mannose receptor (MRC1, CD206) has been historically used as a marker for alternatively activated macrophages[29,30]. Its expression has been shown in human lesions with intraplaque hemorrhage and in thin cap fibroatheromas[31,32], making it a potential

marker of plaque vulnerability. Over the last decades, ^{18}F-FDG has been exploited as a surrogate PET radiotracer for plaque inflammation. Although ^{18}F-FDG is mainly taken up by macrophages[8], other processes than inflammation and other cell types may also contribute to its accumulation in atherosclerotic plaques[33]. Moreover, alternatively activated and inflammatory macrophages have been shown to utilize glucose to a similar extent[34]. In this study, we found a weak correlation between ^{18}F-FDG and ^{64}Cu-MMR uptake measured ex vivo, while no relationship was found between ^{64}Cu-MMR and HDL uptake, which was used to map macrophages by NIRF imaging[35] and did correlate with ^{18}F-FDG uptake. Collectively, these data indicate that different macrophage populations are targeted by these two radiotracers, i.e., all versus CD206^{+} macrophages. Ensuing studies will have to elucidate the complex relationship between inflammation, macrophage phenotype, glucose metabolism and ^{18}F-FDG uptake in the vessel wall.

One of the limitations of atherosclerosis imaging with ^{18}F-FDG is the elevated myocardial uptake, which hinders accurate identification of lesions in the coronary arteries[36]. For comparative purposes, PET-derived aorta-to-heart uptake ratios in diseased rabbits were calculated for ^{18}F-FDG, ^{18}F-NaF and ^{68}Ga-MMR as a measure of their ability to image atherosclerosis in the coronary arteries. Although the MMR nanobody did not show as high a background signal as ^{18}F-FDG, its moderate aorta-to-heart uptake ratio – probably due to the presence of 'background' cardiac resident macrophages[37] – may limit its ability to image coronary plaques to areas with significant macrophage burden. In this respect, ^{18}F-NaF has an enormous advantage, as its cardiac uptake is low. However, in this rabbit model, we had to exclude some aortic regions from our analysis due to elevated ^{18}F-NaF uptake in nearby vertebrae. In the future, this might prevent reliable aortic imaging in patients, while ^{18}F-FDG and ^{68}Ga-MMR showed lower uptake in the vertebrae aside from a marginal uptake in the bone marrow.

In recent years, the community has witnessed a shift in atherosclerosis research towards an integral disease and away from the individual culprit plaque. Monocyte recruitment and local macrophage proliferation have been identified as key processes in atherosclerotic progression, and recent insights indicate some degree of neural involvement[38]. Characterizing all these processes in a longitudinal fashion would enormously benefit from a non-invasive imaging approach. PET is intrinsically a "hot spot" technique and therefore particularly suited to study biological processes systemically[38]. From a clinical perspective, non-invasive imaging has already been successfully used to provide surrogate end points in clinical trials[9]. These often require a large number of participants to ensure a meaningful level of statistical significance is achieved, with long follow-up periods, as the primary end point is typically mortality. Robust non-invasive readouts are therefore extremely beneficial as they directly probe treatment response and thereby provide reliable information in a much shorter timeframe. In this setting, an imaging approach like the one described here can be of great value. Furthermore, the protocol could

be additionally complemented by incorporation of non-contrast T1-weighted (T1W) MRI to investigate the presence of intraplaque hemorrhage or thrombus[39,40], while quantitative evaluation of the fibrous cap and the lipid-rich necrotic core could be performed by T2W-MR imaging[41]. Thus, several specific aspects of the disease can be interrogated simultaneously to obtain a more complete representation of the intervention outcome.

In conclusion, we have translated nanobody-based radiotracer technology to rabbits for the first time and integrated it in a PET/MR imaging protocol that allows evaluation of several key features of atherosclerosis progression. Our protocol enabled reliable phenotyping of rabbit atherosclerotic lesions over time, as well as extensive comparison of the nanobody probes with different clinical radiotracers. Here, we advocate this multiparametric imaging approach that may be used to aid in early-stage drug development as well as in identification of high-risk patients. We believe that the nanobody tracers presented in this study complement the clinically available tracers ^{18}F-FDG and ^{18}F-NaF and, as attested by the phase-I clinical trial of a HER2 nanobody tracer to identify patients with breast cancer[26], their translation is within reach.

References

1. Hansson GK. Inflammation, Atherosclerosis, and Coronary Artery Disease. N Engl J Med 2005;352:1685-95.
2. Robbins CS, Hilgendorf I, Weber GF, et al. Local proliferation dominates lesional macrophage accumulation in atherosclerosis. Nat Med 2013;19:1166-72.
3. Tabas I, Bornfeldt KE. Macrophage Phenotype and Function in Different Stages of Atherosclerosis. Circ Res 2016;118:653-67.
4. Moreno PR, Purushothaman K-R, Sirol M, Levy AP, Fuster V. Neovascularization in Human Atherosclerosis. Circulation 2006;113:2245-52.
5. Narula J, Garg P, Achenbach S, Motoyama S, Virmani R, Strauss HW. Arithmetic of vulnerable plaques for noninvasive imaging. Nat Clin Pract Cardiovasc Med 2008;5:S2-S10.
6. Dweck MR, Aikawa E, Newby DE, et al. Noninvasive Molecular Imaging of Disease Activity in Atherosclerosis. Circ Res 2016;119:330-40.
7. Mulder WJM, Jaffer FA, Fayad ZA, Nahrendorf M. Imaging and Nanomedicine in Inflammatory Atherosclerosis. Sci Transl Med 2014;6:239sr1.
8. Tawakol A, Migrino RQ, Bashian GG, et al. In vivo 18F-fluorodeoxyglucose positron emission tomography imaging provides a noninvasive measure of carotid plaque inflammation in patients. J Am Coll Cardiol 2006;48:1818-24.
9. Fayad ZA, Mani V, Woodward M, et al. Safety and efficacy of dalcetrapib on atherosclerotic disease using novel non-invasive multimodality imaging (dal-PLAQUE): a randomised clinical trial. Lancet 2011;378:1547-59.
10. Joshi N V., Vesey AT, Williams MC, et al. 18F-fluoride positron emission tomography for identification of ruptured and high-risk coronary atherosclerotic plaques: A prospective clinical trial. Lancet 2014;383:705-13.

11. Irkle A, Vesey AT, Lewis DY, et al. Identifying active vascular microcalcification by 18F-sodium fluoride positron emission tomography. Nat Commun 2015;6:7495.
12. Calcagno C, Lobatto ME, Dyvorne H, et al. Three-dimensional dynamic contrast-enhanced MRI for the accurate, extensive quantification of microvascular permeability in atherosclerotic plaques. NMR Biomed 2015;28:1304-14.
13. Dweck MR, Williams MC, Moss AJ, Newby DE, Fayad ZA. Computed Tomography and Cardiac Magnetic Resonance in Ischemic Heart Disease. J Am Coll Cardiol 2016;68:2201-16.
14. Chakravarty R, Goel S, Cai W. Nanobody: The "Magic Bullet" for Molecular Imaging? Theranostics 2014;4:386-98.
15. De Vos J, Mathijs I, Xavier C, et al. Specific Targeting of Atherosclerotic Plaques in ApoE-/- Mice Using a New Camelid sdAb Binding the Vulnerable Plaque Marker LOX-1. Mol Imaging Biol 2014;690-8.
16. Movahedi K, Schoonooghe S, Laoui D, et al. Nanobody-based targeting of the macrophage mannose receptor for effective in vivo imaging of tumor-associated macrophages. Cancer Res 2012;72:4165-77.
17. Broisat A, Hernot S, Toczek J, et al. Nanobodies Targeting Mouse/Human VCAM1 for the Nuclear Imaging of Atherosclerotic Lesions. Circ Res 2012;110:927-37.
18. Falk E, Nakano M, Bentzon JF, Finn AV, Virmani R. Update on acute coronary syndromes: The pathologists' view. Eur Heart J 2013;34:719-28.
19. Mestas J, Ley K. Monocyte-Endothelial Cell Interactions in the Development of Atherosclerosis. Trends Cardiovasc Med 2008;18:228-32.
20. Mehta JL, Sanada N, Hu CP, et al. Deletion of LOX-1 reduces atherogenesis in LDLR knockout mice fed high cholesterol diet. Circ Res 2007;100:1634-42.
21. Gordon S. Alternative activation of macrophages. Nat Rev Immunol 2003;3:23-35.
22. Ishino S, Mukai T, Kuge Y, et al. Targeting of lectinlike oxidized low-density lipoprotein receptor 1 (LOX-1) with 99mTc-labeled anti-LOX-1 antibody: potential agent for imaging of vulnerable plaque. J Nucl Med 2008;49:1677-85.
23. Bala G, Baudhuin H, Remory I, et al. Evaluation of [99mTc]Radiolabeled Macrophage Mannose Receptor-Specific Nanobodies for Targeting of Atherosclerotic Lesions in Mice. Mol Imaging Biol 2018;20:260-7.
24. Getz GS, Reardon C a. Animal models of atherosclerosis. Arterioscler Thromb Vasc Biol 2012;32:1104-15.
25. Iiyama K, Hajra L, Iiyama M, et al. Patterns of Vascular Cell Adhesion Molecule-1 and Intercellular Adhesion Molecule-1 Expression in Rabbit and Mouse Atherosclerotic Lesions and at Sites Predisposed to Lesion Formation. Circ Res 1999;85:199-207.
26. Keyaerts M, Xavier C, Heemskerk J, et al. Phase I study of 68Ga-HER2-Nanobody for PET/CT assessment of HER2-expression in breast carcinoma. J Nucl Med 2015;29:1-29.
27. Derlin T, Toth Z, Papp L, et al. Correlation of Inflammation Assessed by 18F-FDG PET, Active Mineral Deposition Assessed by 18F-Fluoride PET, and Vascular Calcification in Atherosclerotic Plaque: A Dual-Tracer PET/CT Study. J Nucl Med 2011;52:1020-7.
28. Iagaru A, Mittra E, Yaghoubi SS, et al. Novel strategy for a cocktail 18F-fluoride and 18F-FDG PET/CT scan for evaluation of malignancy: results of the pilot-phase study. J Nucl Med 2009;50:501-5.
29. Hirata Y, Tabata M, Kurobe H, et al. Coronary Atherosclerosis Is Associated With Macrophage Polarization in Epicardial Adipose Tissue. J Am Coll Cardiol 2011;58:248-55.

30. Bourlier V, Zakaroff-Girard A, Miranville A, et al. Remodeling Phenotype of Human Subcutaneous Adipose Tissue Macrophages. Circulation 2008;117:806-15.
31. Tahara N, Mukherjee J, de Haas HJ, et al. 2-deoxy-2-[18F]fluoro-D-mannose positron emission tomography imaging in atherosclerosis. Nat Med 2014;20:215-9.
32. Finn AV, Nakano M, Polavarapu R, et al. Hemoglobin directs macrophage differentiation and prevents foam cell formation in human atherosclerotic plaques. J Am Coll Cardiol 2012;59:166-77.
33. Folco EJ, Sheikine Y, Rocha VZ, et al. Hypoxia But Not Inflammation Augments Glucose Uptake in Human Macrophages. J Am Coll Cardiol 2011;58:603-14.
34. Tavakoli S, Short JD, Downs K, et al. Differential Regulation of Macrophage Glucose Metabolism by Macrophage Colony-stimulating Factor and Granulocyte-Macrophage Colony-stimulating Factor: Implications for ^{18} F FDG PET Imaging of Vessel Wall Inflammation. Radiology 2016;283:87-97.
35. Pérez-Medina C, Binderup T, Lobatto ME, et al. In Vivo PET Imaging of HDL in Multiple Atherosclerosis Models. JACC Cardiovasc Imaging 2016;9:950-61.
36. Rosenbaum D, Millon A, Fayad ZA. Molecular imaging in atherosclerosis: FDG PET. Curr Atheroscler Rep 2012;14:429-37.
37. Majmudar MD, Yoo J, Keliher EJ, et al. Polymeric nanoparticle PET/MR imaging allows macrophage detection in atherosclerotic plaques. Circ Res 2013;112:755-61.
38. Tawakol A, Ishai A, Takx RA, et al. Relation between resting amygdalar activity and cardiovascular events: a longitudinal and cohort study. Lancet 2017;389:834-45.
39. Moody A, Allder S, Lennox G, Gladman J, Fentem P. Direct magnetic resonance imaging of carotid artery thrombus in acute stroke. Lancet 1999;353:122-3.
40. Moody AR, Murphy RE, Morgan PS, et al. Characterization of Complicated Carotid Plaque With Magnetic Resonance Direct Thrombus Imaging in Patients With Cerebral Ischemia. Circulation 2003;107:3047-52.
41. Cai J, Hatsukami TS, Ferguson MS, et al. In Vivo Quantitative Measurement of Intact Fibrous Cap and Lipid-Rich Necrotic Core Size in Atherosclerotic Carotid Plaque. Circulation 2005;112: 3437-44.

Methods

Materials

Phospholipids were purchased from Avanti Polar Lipids. The dye 1,1′-dioctadecyl-3,3,3′,3′-tetramethylindodicarbocyanine 4-chlorobenzenesulfonate salt (DiD′) was acquired from Molecular Probes. APOA1 from human plasma was purchased from Athens Research and Technology. All other reagents were acquired from Sigma-Aldrich.

Animal models

All animal experiments were performed in accordance with protocols approved by the Institutional Animal Care and Use Committees of Mount Sinai and/or Memorial Sloan Kettering Cancer Center, and followed National Institutes of Health guidelines for animal welfare.

Mouse model

Female Apoe$^{-/-}$ mice (B6.129P2-Apoe^{tm1Unc}/J, 8-10 weeks old) were purchased from the Jackson Laboratory (Bar Harbor, ME) and fed a cholesterol-enriched, high-fat diet (HFD) (Harlan Teklad TD.88137, 42 % calories from fat) for 20 weeks. Due to the elevated circulating LDL concentrations resulting from their lack of apolipoprotein E, these animals develop atherosclerotic plaques, especially at locations with disturbed flow, i.e. aortic root, and branches of the aortic arch[1,2].

Rabbit model

Male New Zealand White (NZW) rabbits (2.5-3.0 months old) were purchased from Charles River Laboratories (Wilmington, MA). To induce the formation of atherosclerotic plaques, endothelial denudation of the aorta was performed. Anesthesia was induced in rabbits with an intramuscular (i.m.) administration of ketamine (20 mg/kg) (Fort Dodge Animal Health, Overland Park, Kansas, USA) and xylazine (5 mg/kg) (Bayer AG, Leverkusen, Germany). The right femoral artery was identified and used to give access to a 4F-Fogarty embolectomy catheter (Edwards Lifesciences, Irvine, CA) which was inflated at the level of the left subclavian artery and slowly deflated while retracting until the iliac bifurcation, all performed under X-ray guidance (Philips Allura Xper FD20/10, Philips Healthcare, Amsterdam, The Netherlands)[3]. After 4 weeks, the procedure was repeated on the contralateral side. Two weeks before the first surgery a cholesterol diet, regular chow diet enriched with 0.3% cholesterol and 4.7% coconut oil (Research diets, Inc. Brunswick, NJ), was started for a total of 8 weeks. Hereafter the diet was changed to a 0.15% enriched cholesterol diet and continued for the remaining months until the imaging experiments took place. Untreated healthy rabbits were fed a regular chow diet to serve as controls.

Nanobody production and modification with NOTA

The nanobodies cAbVCAM1-5 (VCAM), Lox1.14 (LOX), MMR3.49-NOTAG (MMR) and the control nanobody R3B23, targeting myeloma protein (M-protein), were previously validated, and produced in Escherichia coli as described elsewhere[4-9]. The nanobodies were modified via their lysines with the chelator 1,4,7-triazacyclononane-N,N',N''-triacetic acid (NOTA) following a previously reported procedure[10]. Briefly, a 20 molar excess of the bifunctional chelator 2-S-(4-isothiocyanatobenzyl)-1,4,7-triazacyclononane-N,N',N''-triacetic acid (p-SCN-Bn-NOTA, Macrocyclics) was incubated with 1 mg/mL of the corresponding nanobody dissolved in 0.05 M sodium carbonate buffer (pH 8.7) for 2 h at room temperature. The NOTA-modified nanobody was subsequently purified by size-exclusion chromatography.

In vitro evaluation of unlabeled nanobodies

Extensive in vitro validation of the nanobodies described here has been reported elsewhere[5-7]. The equilibrium dissociation constant ($K_{D,}$ table S1) of the different NOTA-conjugated nanobodies was measured via surface plasmon resonance on a Biacore T200 (GE Healthcare) using the respective immobilized recombinant Fc-protein. Further experimental details were previously described[7,11].

Radiochemistry

^{64}Cu was purchased from Washington University, St. Louis (Washington University School of Medicine Cyclotron, model CS-15, Cyclotron Corp., ^{64}Ni(p,n)^{64}Cu) as [^{64}Cu]$CuCl_2$ with an effective specific activity of 200−400 mCi/μg (7.4−14.8 GBq/μg). ^{68}Ga was eluted from a 50 mCi Eckert & Ziegler Isotope Products (EZIP) ^{68}Ge/^{68}Ga Ionic Gallium Generator IGG100 (Eckert & Ziegler Radiopharma, Hopkinton, MA). The generator was eluted with 0.1 mol/L hydrochloric acid as per the manufacturer's instructions. The ^{68}Ge was measured to be <0.001%.

Radiolabeling

NOTA-modified nanobodies were radiolabeled with Copper-64 (^{64}Cu) to allow extensive ex vivo characterization. A solution of the corresponding nanobody (100 μL, 40-60 μmol/L in 0.1 mol/L NH_4OAc) was diluted with 1 mol/L NH_4OAc buffer (pH = 5, 1 mL). Then, $^{64}CuCl_2$ was diluted in 1 mol/L NH_4OAc buffer (pH = 4.8, 1 mL) and added to the nanobody mixture, and the solution was placed on a thermomixer and shaken at 600 rpm for 10 min at room temperature. After incubation, the labeled nanobody was purified using a pre-conditioned PD10 column (25 mL PBS) and PBS as eluent. The radiochemical yield was > 90% (91 ± 6 %, n = 8). Radiochemical purity was > 97%, as assessed by size exclusion radio-HPLC (figure 1D).

The same NOTA-modified MMR nanobody was radiolabeled with ^{68}Ga. A solution of the corresponding nanobody (100 μL, 40-60 μmol/L in 0.1 mol/L NH_4OAc) was diluted with 1 mol/L NaOAc buffer (pH = 4.8, 1 mL). Then, $^{68}GaCl_3$ in 0.1 mol/L HCl (1.5 mL) was added to the reaction mixture (pH = 4.8), and the solution was placed in a thermomixer and shaken at 600 rpm for 10 min at 50 °C. After incubation, the ^{68}Ga-labeled nanobody was purified using a pre-conditioned PD10 column (equilibrated with 25 mL PBS) and PBS as eluent. The radiochemical yield was 81 ± 6 % (n = 6) and the radiochemical purity > 98%, as assessed by size exclusion radio-HPLC (figure 1D).

Radio-HPLC. HPLC was performed on a Shimadzu HPLC system equipped with two LC-10AT pumps, an SPD-M10AVP photodiode array detector a Lablogic Scan-RAM Radio-TLC/HPLC detector. Size exclusion chromatography was performed on a Superdex 75 5/150 GL (GE Healthcare Life Sciences, Pittsburgh, PA) using PBS as eluent at a flow rate of 0.2 mL/min.

MicroPET/CT imaging

Apoe$^{-/-}$ mice (n = 14, weight: 25.2 ± 1.2 g) were injected with the corresponding nanobody radiotracer (0.20-0.30 mCi) in 200 µL PBS solution via the lateral tail vein. One hour post injection (p.i.), animals were anesthetized with isoflurane (Baxter Healthcare, Deerfield, IL)/oxygen gas mixture (2% for induction, 1 % for maintenance), and a scan was then performed using an Inveon microPET/CT scanner (Siemens, Malvern, PA). Whole body PET static scans recording a minimum of 50 million coincident events were performed, with duration of 15 min. The energy and coincidence timing windows were set at 350−700 keV and 6 ns, respectively. The image data was normalized to correct for non-uniformity of response of the PET, dead-time count losses, positron branching ratio, and physical decay to the time of injection, but no attenuation, scatter, or partial-volume averaging correction was applied. The counting rates in the reconstructed images were converted to activity concentrations (%ID/g) by use of a system calibration factor derived from the imaging of a mouse-sized water-equivalent phantom containing the radionuclide. Images were analyzed using Inveon Research Workplace software (Siemens, Malvern, PA). Whole body standard low magnification CT scans will be performed with the X-ray tube setup at a voltage of 80 kV and current of 500 µA. The CT scan will be acquired using 120 rotational steps for a total of 220 degrees yielding an estimated scan time of 120 s with an exposure of 145 ms per frame. After the scan, animals were sacrificed and perfused, and tissues (brain, heart, lungs, aorta, spleen, liver, kidneys, skeletal muscle and bone) collected, blotted and weighed in pre-weighed tubes. Radioactivity content was measured by gamma counting, and tissue radioactivity concentration was calculated and expressed as %ID/g.

Pharmacokinetics and biodistribution in mice

Apoe$^{-/-}$ mice (n = 17, weight: 30.0 ± 5.7 g) were randomly divided in 5 groups and injected with the corresponding ^{64}Cu-nanobody (25 ± 8 µCi) via the lateral tail vein. Blood radioactivity half-life was determined by serial blood draws from the tail vein at 1, 5, 10, 20, 40, 60, 120 and 180 minutes after injection. Blood was weighed and counted using a Wizard^{2} 2480 automatic gamma counter (Perkin Elmer, Waltham, MA). At 3 hours after injection, all mice were sacrificed by isofluorane (Baxter, Deerfield, IL) overdose followed by cervical dislocation, and perfused with 20 mL saline. Tissues were harvested (brain, heart, lungs, aorta, spleen, liver, kidneys, skeletal muscle and bone) and weighed before radioactivity counting. The values were corrected for decay and radioactivity concentration in tissues was calculated as percentage of injected dose per gram (%ID/g). Data shown in Figure S7 were obtained from Apoe$^{-/-}$ mice (n = 14) injected with the corresponding ^{64}Cu- or ^{68}Ga-labeled nanobody (0.20-0.30 mCi) and sacrificed 60 minutes post injection.

Fluorescent reconstituted high-density lipoprotein (rHDL) nanoparticles Fluorescent HDL nanoparticles were prepared by incorporation of the near infrared fluorescence (NIRF) dye DiD' following a previously described method with modifications[12]. Briefly, phospholipids 1,2-dimyristoyl-sn-glycero-3-phosphocholine (DMPC) and 1-myristoyl-2-hydroxy-sn-glycero-3-phospho-(1'-rac-glycerol) sodium salt (MHPC) were mixed in chloroform at a 12:1 weight ratio. DiD' was then added to achieve a 92:8 phospholipid-to-dye weight ratio. A thin film was formed by evaporation of the solvent, and large vesicles were made by hydrating the film with an APOA1 solution (5 mg per mg of dye). Subsequent sonication, centrifugation and filtration yielded a clear solution containing small rHDL particles (mean effective diameter 7-9 nm). This formulation was used as an atherosclerotic plaque/macrophage mapping NIRF agent. Rabbits were injected with fluorescent rHDL (~1 mg dye/rabbit) 24 h prior to the nanobody PET/MRI scan.

PET/MR imaging

NZW male rabbits (n = 31, mean weight 3.40 ± 0.30 kg) received an intramuscular injection of ketamine (20 mg/kg) with xylazine (5 mg/kg) to induce anesthesia. Intravenous (i.v.) catheters were placed in the right (24G) and in the left (22G) marginal ear veins. In both central ear arteries 24G-catheters were placed for blood withdrawal. The bladder was emptied using a pediatric (8 Fr.) urine catheter (Bard Catheters) and a urine collection bag was attached for the duration of the whole scan to prevent any disruption from bladder signal.

A clinical 3 Tesla Biograph mMR (Siemens, Erlangen, Germany) was used for the PET/MRI studies. Rabbits were placed in a flexible human body matrix coil (Siemens) on the scanner bed under isoflurane anesthesia at 1.5% by inhalation, and were oxygenated for the remaining of the PET/MR imaging experiment. Vital parameters were monitored. ^{64}Cu-nanobodies (39.6 ± 10.3 MBq, n = 19) were i.v. injected shortly before the start of the PET scan and images were acquired in a dynamic fashion for 170 minutes. For ^{68}Ga-MMR (128 ± 31 MBq, n = 12), a static PET scan was performed 120 minutes after injection.

After scout scans, the PET scan was initiated and acquired simultaneously with bright-blood time-of-flight (TOF) non-contrast enhanced angiography for localization of arterial anatomical landmarks (renal arteries and iliac bifurcation). Imaging parameters were: repetition time (TR), 23 ms; echo time (TE), 2.8 ms; flip angle, 20 degrees; spatial resolution, 0.35 mm^2 (interpolated); slice thickness, 1 mm. Attenuation correction of PET images was performed by segmenting a vendor built-in two-point Dixon MR-based attenuation correction (MR-AC) sequence into 2 tissue compartments (soft tissue and air). Images were reconstructed using a 3D ordinary Poisson ordered subsets expectation maximization (OP-OSEM) algorithm with point-spread-function (PSF) resolution modeling, using 3 iterations and 21 subsets. Simultaneously a black blood 3D T2 weighted

Sampling Perfection with Application optimized Contrasts using different flip angle Evolution (SPACE) sequence was used for vessel wall delineation. Imaging parameters were: TR, 1600 ms; TE, 115 ms; flip angle, 120 degrees; echo train length (ETL), 81; spatial resolution, 0.63 mm^2; slice thickness, 0.63 mm; fat saturation on. For Dynamic contrast enhanced (DCE) MRI a segmented fast low angle shot (FLASH) sequence was used, with motion sensitized drive equilibrium (MSDE) preparation to obtain black blood. Imaging parameters were: TR, 491 ms; TE, 5.3 ms; flip angle, 20 degrees; spatial resolution, 0.63 mm^2; slice thickness, 0.63 mm; fat saturation, on. DCE-MRI was acquired before, during and after the injection of 0.4 mmol/kg of Gd-DTPA (Magnevist, Bayer). 20 dynamic frames were acquired, for a total scan duration of 10 minutes and 58 seconds, yielding a time resolution per frame of approximately 33 seconds. The same sequence was also acquired before and after DCE-MRI, with the same imaging parameters except for signal averages (4 instead of 1 for DCE-MRI), for delayed enhancement (DE) imaging. This black blood DCE-MRI protocol is explained in more detail elsewhere[13,14].

^{18}F-FDG and ^{18}F-NaF PET static scans

For a direct comparison, all rabbits were imaged with ^{18}F-FDG two days prior to the nanobody-PET scan. Animals were injected with ^{18}F-FDG (161 ± 45 MBq, n = 31) through a catheter in the marginal ear vein. A urine catheter was used, as explained above. The radiotracer was allowed to circulate for at least 3 hours before a static PET/MRI scan was performed, for the duration of 20 minutes. In addition, an ^{18}F-sodium fluoride scan was included in the progression study. Three days prior to the ^{68}Ga-MMR-PET scan, animals were injected with ^{18}F-NaF (182 ± 21 MBq, n = 11) via the marginal ear vein. All doses were approximately half the amount of a clinical dose. A static PET/MRI scan was performed approximately 90 minutes after tracer injection, for the duration of 20 min. These static scans included a TOF non-contrast enhanced angiography for localization of arterial anatomical landmarks (renal arteries and iliac bifurcation), and MR-AC for attenuation correction of the PET images using the same parameters listed above.

Image analysis

All DCE-MRI images were reformatted in the axial plane for tracing. The vessel wall tracing was carried out on the average image of the DCE-MRI dynamic series using Osirix (5.6) software (OsiriX Foundation, Geneva, Switzerland). Vessel wall area or regions of interest (ROI) were measured by manually drawing an inner and an outer vessel wall contour and computing the difference between these two. The area under the normalized signal intensity curve (IAUC) was calculated at two minutes after contrast agent (CA) administration, serving as a time point for data analysis with a custom made program written in Matlab (Mathworks, Natick, MA)(http://www.mathworks.com). IAUC is a measure of CA accumulation in the (atherosclerotic) vessel wall. IAUC was calculated on a

pixel-by-pixel basis. MR signal intensity over time was normalized to vertebral muscle signal intensity before CA injection.

PET imaging analysis was performed after all data had been processed and divided in different time frames using a custom made program written in Matlab. All data were subsequently processed using OsiriX by manually drawing ROIs on the infrarenal abdominal aorta and tissues of interest (liver, spleen, bone marrow and kidneys). Standardized uptake values (SUVs, defined as [Pixel value (Bq/mL) * Weight of the subject (kg) / Dose (Bq)] * 1000 g/kg) were obtained by averaging SUV_{max} values in each ROI drawn on all slices over the whole organ or over at least 10 slices of the tissue of interest. For comparison between the different parameters (nanobody uptake, ^{18}F-FDG uptake, ^{18}F-NaF uptake, T2W-MRI vessel wall area, and 3D DCE-MRI permeability indices) the abdominal aorta was divided in 10 equal segments, from left renal artery to iliac bifurcation, and their associated values were averaged. The same segments were used for comparison with HDL NIRF and autoradiography data.

Pharmacokinetics and biodistribution in rabbits

For pharmacokinetic analysis, blood was sampled via the central ear arteries using 24G-catheters at 1, 5, 10, 20, 40, 60, 120, 170 and 240 min post injection (p.i.). Blood was weighed and its radioactivity content measured by gamma counting (Perkin Elmer, Waltham, MA). Radioactivity distribution measurements were performed after the end of the last scan (4 h p.i.). Rabbits were sacrificed by pentobarbital overdose and extensively perfused with at least 500 mL of saline. Tissues (heart, aorta, lungs, spleen, liver, kidneys, skeletal muscle, bone marrow and bone) were collected, blotted and diced before weighing and gamma counting. The values were corrected for decay and radioactivity concentration in tissues was calculated as percentage of injected dose per gram (%ID/g).

Near-infrared fluorescence imaging

Shortly after sacrifice, perfused aortas were placed on thick black paper and imaged on a Xenogen IVIS Spectrum Preclinical Imaging System (Perkin Elmer, Waltham, MA). Fluorescence images were acquired with a selected excitation and emission band-pass filter corresponding to Cy5.5/DiD' (λ_{Exc} = 640 ± 18 nm, λ_{Em} = 720 ± 10 nm). Exposure time for each image was 2 s. Data were processed and analyzed using Living Image software (Perkin Elmer) by drawing ROIs around the aortas, and quantified as radiant efficiency.

Histological analysis and immunohistochemistry

Sections from mouse and rabbit aortas were cut immediately after sacrifice to allow autoradiographic analysis. For mice, the aortic root was embedded in optimal cutting temperature (OCT) compound, frozen and cut in 6-µm sections. One section was used for autoradiography and the adjacent/consecutive sections were used for immunhisto-

chemistry. Staining with hematoxylin and eosin (H&E), and immunostaining for CD68 (macrophages) and CD31 (endothelial cells) was performed. Similarly, rabbit aortic fragments (~0.5 cm thick) were embedded in OCT compound, frozen and cut (20 μm thick for autoradiography and 7 μm for stained sections) as explained above. Staining with (H&E) and von Kossa (microcalcifications), and immunostaining for RAM-11 (macrophages) and CD206 (macrophage mannose receptor) was performed using similar methods as described before and using manufacturer's protocols[13]. Correlations were computed by comparing the mean gray intensity values of the masks created using ImageJ software (NIH) for autoradiography and adjacent stained sections.

Autoradiography

Digital autoradiography was performed to determine radiotracer distribution within the aorta. Samples were placed in a film cassette against a phosphorimaging plate (BASMS-2325, Fujifilm, Valhalla, NY) for 87 h (mouse aortas), 24 h (rabbit aortas) and 17 h (aortic sections) at -20 °C. Phosphorimaging plates were read at a pixel resolution of 25 μm with a Typhoon 7000IP plate reader (GE Healthcare, Pittsburgh, PA). Quantification was carried out using ImageJ software by dividing the aorta in 10 sections that were compared against aortic portions of equal length applied to the images obtained by PET/MRI.

Statistics

Data are presented as median with interquartile range (IQR). Differences were evaluated using Mann-Whitney test (between 2 groups) or Kruskal-Wallis followed by Dunn's test for multiple comparisons (for 3 or more groups). For all tests, $P < 0.05$ represents statistical significance. Spearman's r coefficient was calculated to determine correlation, using the Bonferroni correction for multiple comparisons. Statistical analyses were performed with GraphPad Prism®, Version 6.0c (La Jolla, CA).

References

1. Plump AS, Smith JD, Hayek T, et al. Severe hypercholesterolemia and atherosclerosis in apolipoprotein E-deficient mice created by homologous recombination in ES cells. *Cell* 1992;71:343-53.
2. Nakashima Y, Plump AS, Raines EW, Breslow JL, Ross R. ApoE-deficient mice develop lesions of all phases of atherosclerosis throughout the arterial tree. *Arterioscler Thromb* 1994;14:133-40.
3. Lobatto ME, Calcagno C, Metselaar JM, et al. Imaging the Efficacy of Anti-Inflammatory Liposomes in a Rabbit Model of Atherosclerosis by Non-Invasive Imaging. *Methods Enzymol* 2012;508:211-28.

4. Saerens D, Pellis M, Loris R, et al. Identification of a Universal VHH Framework to Graft Non-canonical Antigen-binding Loops of Camel Single-domain Antibodies. *J Mol Biol* 2005;352:597-607.
5. Arbabi Ghahroudi M, Desmyter A, Wyns L, Hamers R, Muyldermans S. Selection and identification of single domain antibody fragments from camel heavy-chain antibodies. *FEBS Lett* 1997;414:521-26.
6. Conrath KE, Lauwereys M, Galleni M, et al. Lactamase Inhibitors Derived from Single-Domain Antibody Fragments Elicited in the Camelidae. *Antimicrob Agents Chemother* 2001;45:2807-12.
7. Broisat A, Hernot S, Toczek J, et al. Nanobodies Targeting Mouse/Human VCAM1 for the Nuclear Imaging of Atherosclerotic Lesions. *Circ Res* 2012;110:927-37.
8. De Vos J, Mathijs I, Xavier C, et al. Specific Targeting of Atherosclerotic Plaques in ApoE-/- Mice Using a New Camelid sdAb Binding the Vulnerable Plaque Marker LOX-1. *Mol Imaging Biol* 2014;16:690-8.
9. Blykers A, Schoonooghe S, Xavier C, et al. PET Imaging of Macrophage Mannose Receptor-Expressing Macrophages in Tumor Stroma Using 18F-Radiolabeled Camelid Single-Domain Antibody Fragments. *J Nucl Med* 2015;56:1265-71.
10. Xavier C, Vaneycken I, D'huyvetter M, et al. Synthesis, preclinical validation, dosimetry, and toxicity of 68Ga-NOTA-anti-HER2 Nanobodies for iPET imaging of HER2 receptor expression in cancer. *J Nucl Med* 2013;54:776-84.
11. Movahedi K, Schoonooghe S, Laoui D, et al. Nanobody-based targeting of the macrophage mannose receptor for effective in vivo imaging of tumor-associated macrophages. *Cancer Res* 2012;72:4165-77.
12. Pérez-Medina C, Binderup T, Lobatto ME, *et al*. InVivo PET Imaging of HDL in Multiple Atherosclerosis Models. *JACC Cardiovasc Imaging* 2016;9:950-61.
13. Calcagno C, Cornily J-C, Hyafil F, et al. Detection of neovessels in atherosclerotic plaques of rabbits using dynamic contrast enhanced MRI and 18F-FDG PET. *Arterioscler Thromb Vasc Biol* 2008;28:1311-7.
14. Calcagno C, Lobatto ME, Dyvorne H, et al. Three-dimensional dynamic contrast-enhanced MRI for the accurate, extensive quantification of microvascular permeability in atherosclerotic plaques. *NMR Biomed* 2015;28:1304-14.
15. Taylor ME. Structure and Function of the Macrophage Mannose Receptor. In: Crocker PR, ed. *Mammalian Carbohydrate Recognition Systems.* Berlin, Germany: Springer Berlin Heidelberg; 2001:105-21.

Supplementary figures

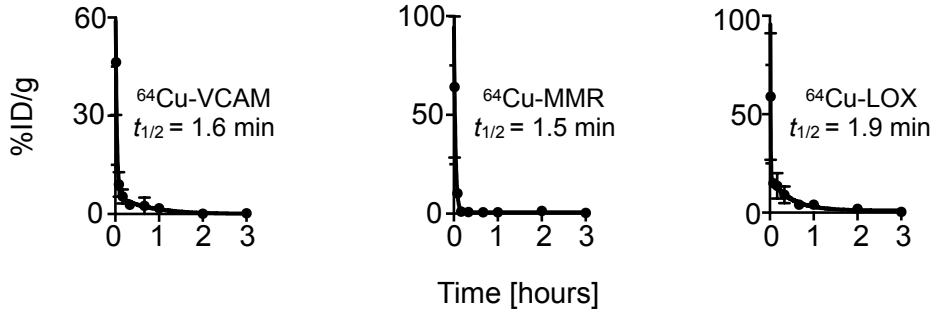

Figure S1. ^{64}Cu-nanobody pharmacokinetics in Apoe$^{-/-}$ mice. Time-activity curves for all ^{64}Cu-nanobodies in Apoe$^{-/-}$ mice.

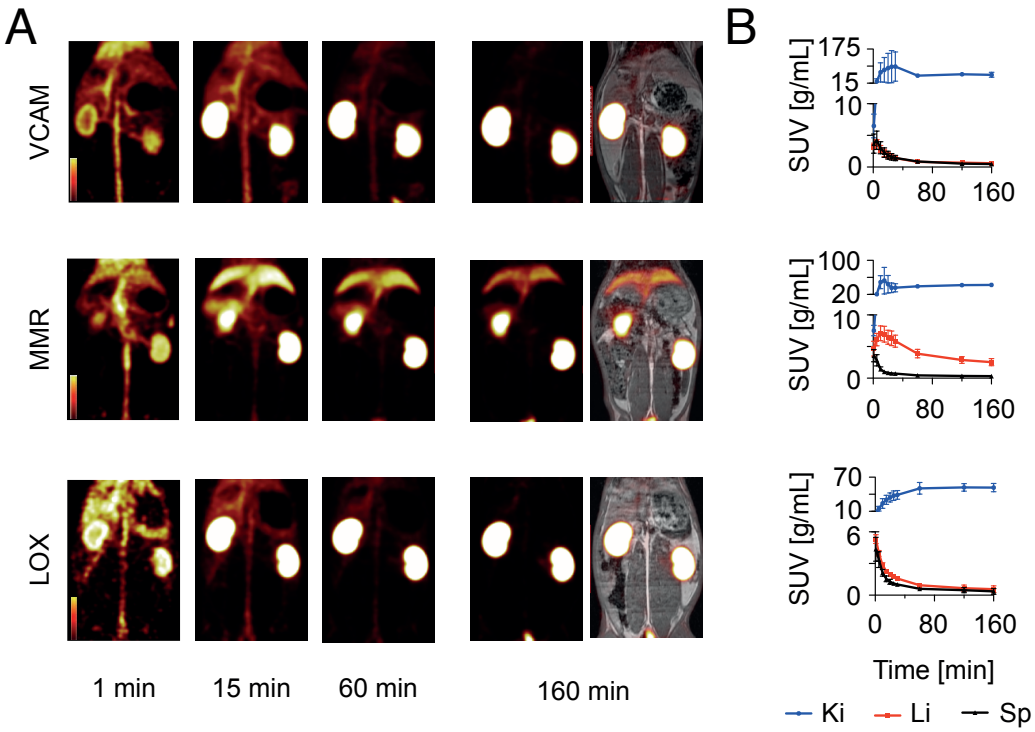

Figure S2. Whole-body PET/MR imaging of ^{64}Cu-labeled nanobodies in rabbits with atherosclerosis. PET imaging data were acquired in a dynamic fashion for 170 min directly after injection to allow in vivo biodistribution evaluation, and segmented for analysis. A) Representative coronal PET images at 1, 15, 60, 160 min, and fused coronal PET/MR image at 160 min p.i. of ^{64}Cu-VCAM, ^{64}Cu-MMR and ^{64}Cu-LOX, from top to bottom (n ≥ 4 per nanobody), and B) corresponding PET radioactivity quantification data in organs of interest in atherosclerotic rabbits (1-170 min, n ≥ 4 per nanobody). Similar to the mouse studies, rapid radioactivity accumulation in the kidneys gave rise to an intense signal that gradually plateaued at an SUV of ~50 g/mL. PET signal from liver and spleen was initially moderate and gradually decreased to low SUV < 1 g/mL at 60 min p.i., except in animals injected with ^{64}Cu-MMR, which had an SUV > 2.5 g/mL over the full length of the scan, likely indicating specific uptake by hepatic mannose receptor (CD206)-expressing cells[15]. Ki: kidney, Li: liver, Sp: spleen.

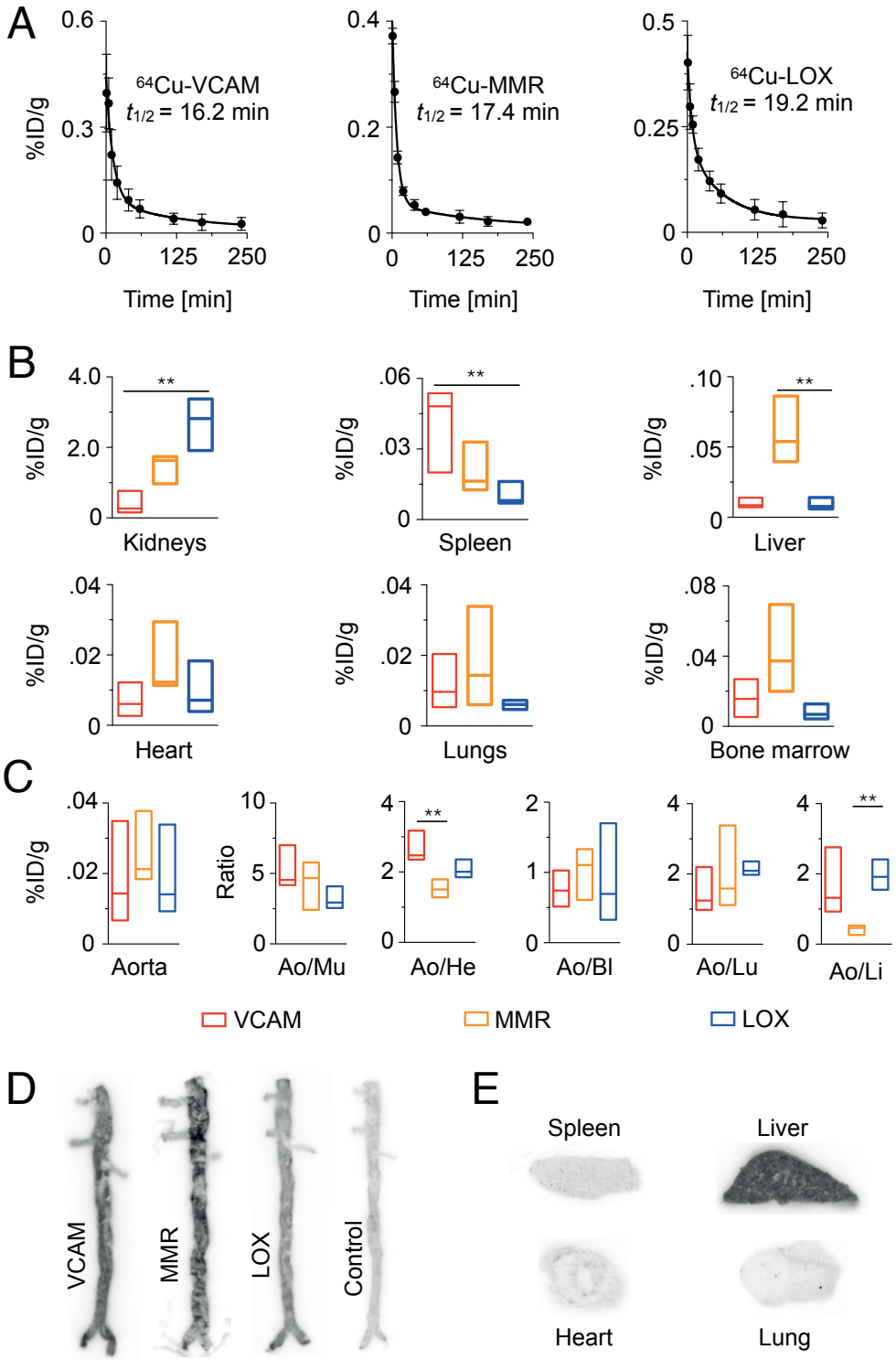

Figure S3. Pharmacokinetics and biodistribution of ^{64}Cu-nanobodies in rabbits with atherosclerosis. A) Blood time-activity curves, and B) radioactivity distribution in selected tissues -measured by gamma counting- in rabbits with atherosclerosis (4 months on high-fat diet) 4 h p.i. of the corresponding ^{64}Cu-nanobody (n ≥ 4 per nanobody). C) Quantification of radioactivity by gamma counting of atherosclerotic rabbit aortas, aorta-to-muscle, aorta-to-heart, aorta-to-blood, aorta-to-lung and aorta-to-liver ratios 4 h p.i. of the corresponding ^{64}Cu-nanobody (n ≥ 4 per nanobody). D) Representative autoradiography of abdominal atherosclerotic rabbit aortas and of, E) spleen, liver, heart and lung from rabbits injected with ^{64}Cu-MMR. * P < 0.05. ** P < 0.01.

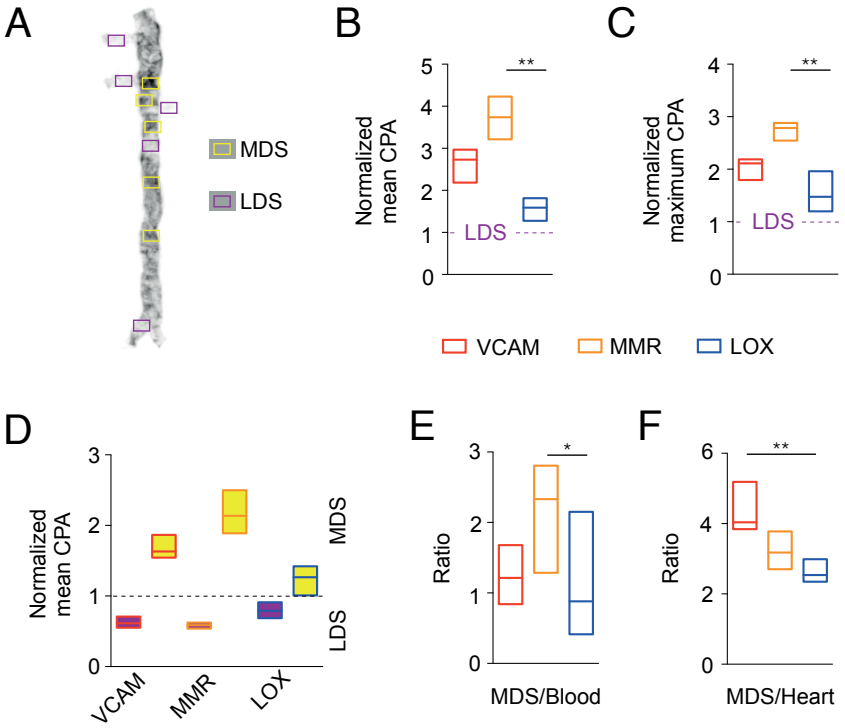

Figure S4. Autoradiographic analysis of rabbit atherosclerotic aortas. A) Regional radioactivity deposition in atherosclerotic aortas after injection of ^{64}Cu-nanobodies was quantified ex vivo by autoradiography. Five regions of interest (ROIs) were drawn on sites of high (most diseased segment, MDS) and low (least diseased segment, LDS) radioactivity accumulation to quantify mean and maximum counts per unit area (CPA). Three LDS ROIs were always drawn on aortic branches for all aortas (n = 5 per nanobody tracer), as this tissue was not affected by the endothelial denudation procedure. MDS CPA normalized to LDS (dashed line) based on B) mean, and C) maximum ROI values. D) Comparison of LDS (purple-filled boxes) and MDS (yellow-filled boxes) values relative to mean CPA for whole abdominal aorta (dashed line) based on mean ROI values. An MDS correction factor based on the median value in the yellow-filled boxes can be derived from this analysis. Applying this MDS factor to the values presented in figure S3C, E) MDS-to-blood, and F) MDS-to-heart ratios can be obtained. * $P < 0.05$. ** $P < 0.01$.

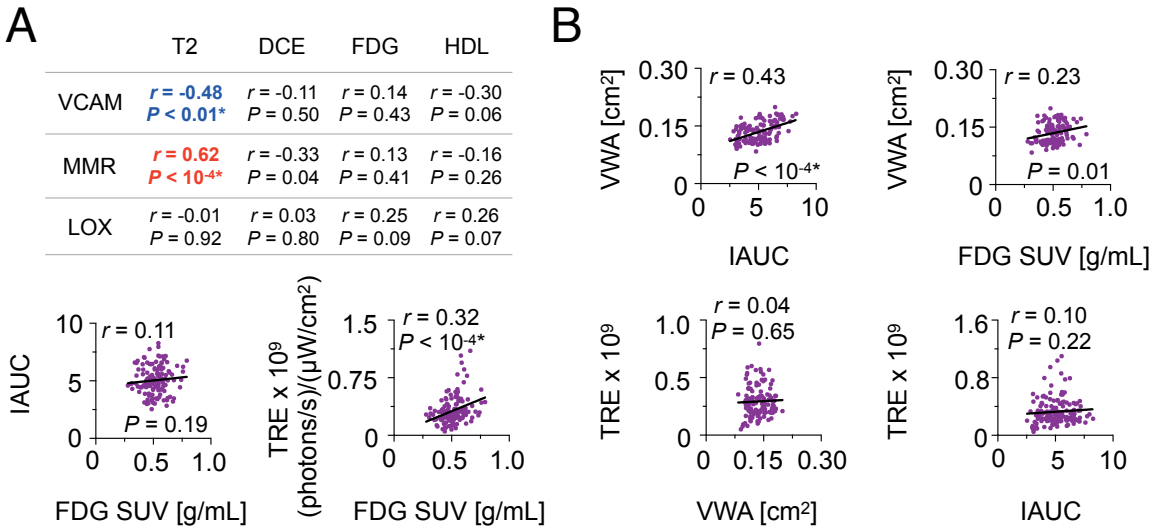

Figure S5. Non-invasive imaging-guided characterization of rabbit atherosclerotic aortas. Given the focal nature of atherosclerosis, we carried out a region-by-region analysis to accurately identify potential associations between the different features under study. Thus, PET and MRI abdominal aorta images were divided in ten equal regions, from the left renal artery to the iliac bifurcation, and the obtained values for the different parameters were compared against each other. A) Heat map (red is positive, blue is negative) showing degree of correlation between PET-derived ^{64}Cu-nanobody uptake and T2-weighted MRI (T2W-MRI) vessel wall area (VWA), DCE-MRI's intensity area under the curve (IAUC), PET-derived ^{18}F-FDG uptake and DiD-HDL near-infrared fluorescence-measured total radiant efficiency (TRE). B) To gain a deeper understanding of our rabbit atherosclerosis model, we also performed a comparative analysis between T2W-MRI VWA, DCE-MRI's IAUC, ^{18}F-FDG-PET and DiD-HDL NIRF including all rabbits in the ^{64}Cu-nanobody study. A significant positive correlation was found between vessel wall area and both permeability and ^{18}F-FDG uptake, whereas no association was apparent between permeability and ^{18}F-FDG uptake. Overall, DiD-HDL NIRF intensity positively correlated with ^{18}F-FDG uptake, but not with vessel wall area or permeability, while the correlation with any of the nanobodies was absent or weak. *Statistically significant after applying the Bonferroni correction for multiple comparisons.

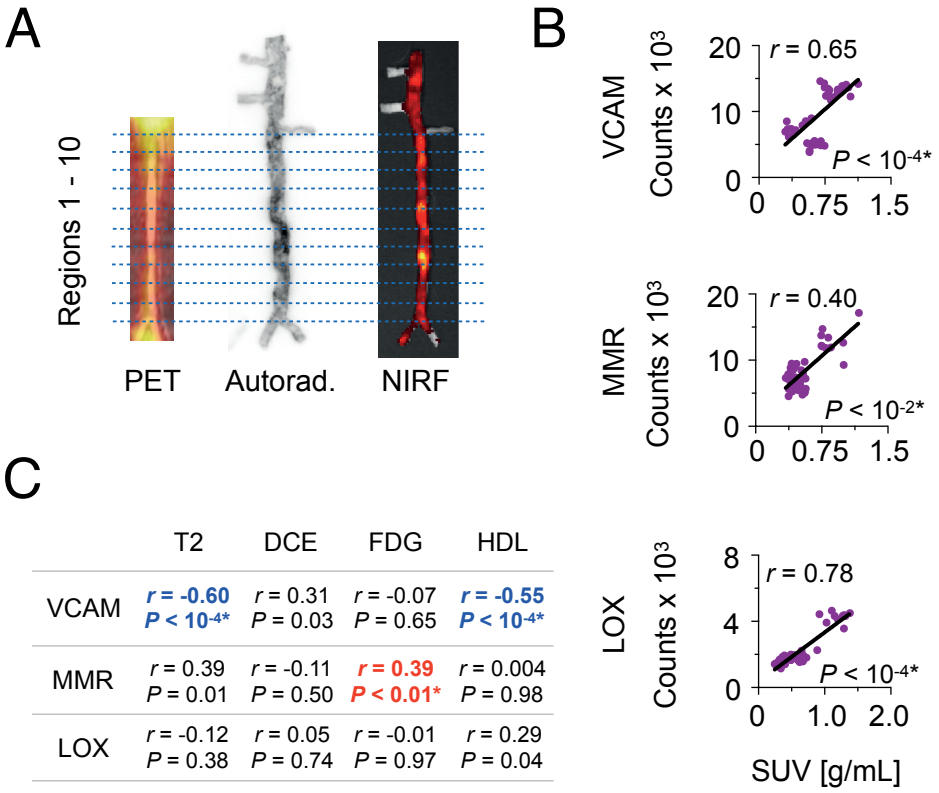

C

	T2	DCE	FDG	HDL
VCAM	**r = -0.60 $P < 10^{-4}$***	r = 0.31 P = 0.03	r = -0.07 P = 0.65	**r = -0.55 $P < 10^{-4}$***
MMR	r = 0.39 P = 0.01	r = -0.11 P = 0.50	**r = 0.39 $P < 0.01$***	r = 0.004 P = 0.98
LOX	r = -0.12 P = 0.38	r = 0.05 P = 0.74	r = -0.01 P = 0.97	r = 0.29 P = 0.04

Figure S6. Ex vivo characterization of rabbit atherosclerotic aortas. A) We performed a similar analysis using autoradiography data. The autoradiographs of abdominal aortas were divided in ten equal regions, from the left renal artery to the iliac bifurcation, and their associated radioactivity was quantified. B) Importantly, in vivo uptake measured by PET and radioactivity accumulation as determined from the autoradiographs were significantly correlated for all three ^{64}Cu-nanobodies, demonstrating the reliability of the imaging-derived values. C) Heat map (red is positive, blue is negative) showing degree of correlation between autoradiography-derived ^{64}Cu-nanobody radioactivity deposition in atherosclerotic aortas and T2-weighted MRI vessel wall area, DCE-MRI's intensity area under the curve, PET-derived ^{18}F-FDG uptake and DiD-HDL near-infrared fluorescence-measured total radiant efficiency values. *Statistically significant after applying the Bonferroni correction for multiple comparisons.

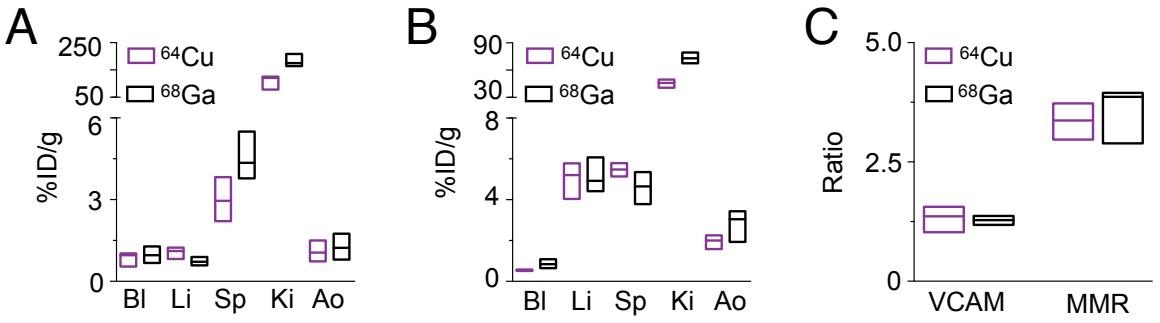

Figure S7. Comparison between ^{64}Cu- and ^{68}Ga-labeled nanobodies in Apoe$^{-/-}$ mice. Radioactivity distribution in selected tissues in Apoe$^{-/-}$ mice at 1 h p.i. of A) ^{64}Cu- and ^{68}Ga-VCAM nanobody (n ≥ 3), and B) and ^{64}Cu- and ^{68}Ga-MMR nanobody (n ≥ 3). C) Aorta-to-blood ratios for both ^{64}Cu and ^{68}Ga labeled VCAM and MMR nanobodies.

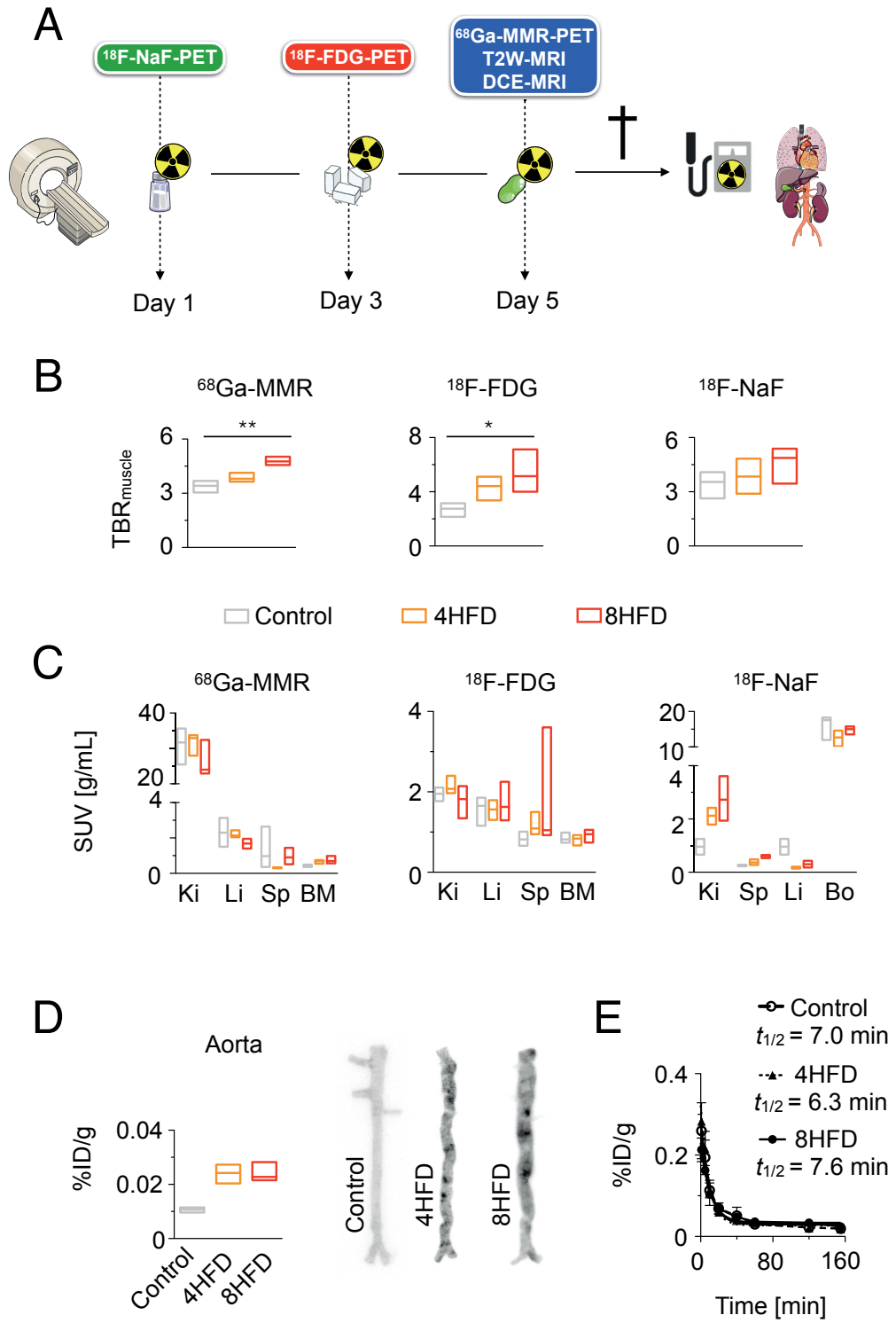

Figure S8. PET/MR imaging evaluation of atherosclerosis progression. A) Rabbit PET/MR imaging schedule. B) PET-derived aorta-to-muscle ratios and, C) radioactivity distribution in selected tissues for ^{68}Ga-MMR (left), ^{18}F-FDG (middle) and ^{18}NaF (right), showing data for control (grey) and atherosclerotic rabbits that had been 4 and 8 months on high-fat diet (4HFD, red, and 8HFD, green, respectively). D) Radioactivity quantification of atherosclerotic rabbit aortas by gamma counting 2.5 h p.i. of ^{68}Ga-MMR (n ≥ 3), and representative autoradiographs from the three groups. E) Blood time-activity curve for ^{68}Ga-MMR in control and atherosclerotic rabbits. Ki = kidneys, Li = liver, SP = spleen, BM = bone marrow, Bo = bone. * P < 0.05. ** P < 0.

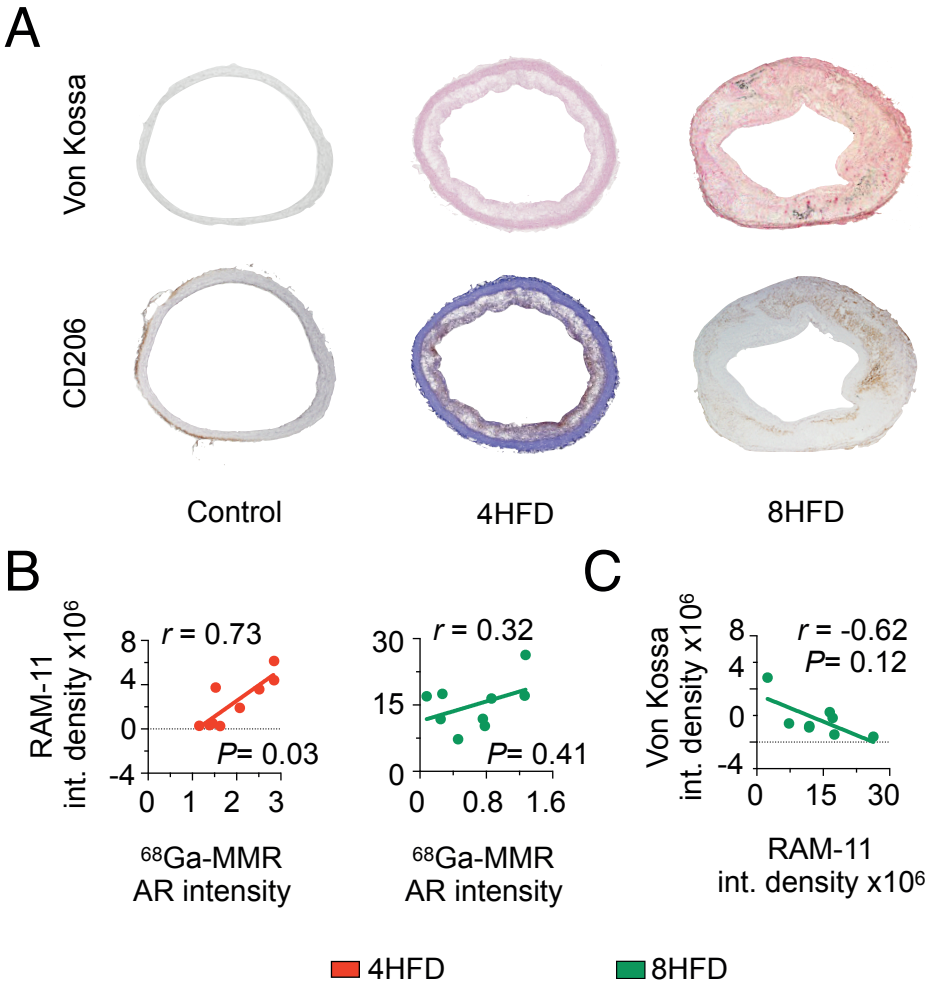

Figure S9. Immunohistochemical analysis of atherosclerosis progression. A) Representative images of healthy control and atherosclerotic rabbit aortic sections showing Von Kossa (microcalcifications) and CD206 (MMR-expressing macrophages) staining. B) Correlation between ^{68}Ga-MMR autoradiography and RAM-11 staining (macrophages) in aortic sections from rabbits that had been 4 (red, left) or 8 months (green, right) on cholesterol-enriched high-fat diet. C) Correlation between Von Kossa and RAM-11 staining, quantified as integrated density (ID) in aortic sections from rabbits that had been 8 months on cholesterol-enriched high-fat diet.

Table S1. Equilibrium dissociation constants of the nanobodies used in this study.

	K_D (nanobody)	K_D (NOTA-nanobody)
VCAM	21.6 ± 1.2 nM	23.6 ± 0.8 nM
MMR	18.3 ± 1.4 nM	21.4 ± 1.0 nM
LOX	34.2 ± 1.1 nM	32.9 ± 1.2 nM

Table S2. Tissue radioactivity distribution in Apoe$^{-/-}$ mice at 3 hours p.i. of the corresponding ^{64}Cu-nanobody. Data are expressed as percent of injected dose per gram ± standard deviation (n ≥ 3 per nanobody).

	VCAM	MMR	LOX	Control
Aorta	0.24 ± 0.04	1.2 ± 0.3	0.70 ± 0.38	0.41 ± 0.04
Blood	0.21 ± 0.07	0.37 ± 0.04	0.27 ± 0.04	0.42 ± 0.06
Bone	0.55 ± 0.30	1.1 ± 0.13	0.44 ± 0.19	0.29 ± 0.08
Brain	0.003 ± 0.003	0.03 ± 0.03	0.04 ± 0.01	0.04 ± 0.01
Heart	0.006 ± 0.004	0.89 ± 0.13	0.21 ± 0.07	0.27 ± 0.04
Kidney	111 ± 28	46 ± 13	96 ± 8	75 ± 10
Liver	0.53 ± 0.19	3.8 ± 0.7	0.90 ± 0.29	1.1 ± 0.2
Lungs	0.30 ± 0.22	0.30 ± 0.22	0.61 ± 0.41	0.6 ± 0.3
Muscle	0.03 ± 0.01	0.47 ± 0.01	0.20 ± 0.07	0.10 ± 0.03
Spleen	1.9 ± 0.4	4.0 ± 0.6	0.26 ± 0.07	0.33 ± 0.04

Table S3. Key imaging parameters for the three radiotracers included in the atherosclerosis progression study. Data are expressed as median with interquartile range (n ≥ 3 per nanobody). TBR: target-to-background ratio, in this case aorta/muscle ratio.

		^{18}F-FDG	^{68}Ga-MMR	^{18}F-NaF
	Target	Inflammation/hypoxia	Macrophages	Microcalcifications
	Time of scan	180 min p.i.	120 min p.i.	90 min p.i.
SUV_{max}	Control	0.32 (0.28-0.35)	0.23 (0.21-0.26)	0.21 (0.20-0.22)
	4HFD	0.53 (0.39-0.59)	0.36 (0.33-0.39)	0.27 (0.24-0.30)
	8HFD	0.65 (0.57-0.78)	0.46 (0.42-0.50)	0.64 (0.45-0.71)
TBR	Control	2.8 (2.2-3.2)	3.4 (3.1-3.6)	3.5 (2.6-4.1)
	4HFD	4.4 (3.5-5.1)	3.8 (3.7-4.1)	3.8 (3.1-4.6)
	8HFD	5.2 (4.3-6.6)	4.7 (4.6-5.0)	4.9 (3.8-5.3)
	Aorta/heart ratio	0.3 (0.2-0.3)	0.7 (0.6-0.8)	1.1 (1.0-1.2)